STRUCTURAL BIOLOGY

Structural insights into the assembly of gp130 family cytokine signaling complexes

Yi Zhou*, Panayiotis E. Stevis, Jing Cao, Kei Saotome, Jiaxi Wu, Arielle Glatman Zaretsky, Sokol Haxhinasto, George D. Yancopoulos, Andrew J. Murphy, Mark W. Sleeman, William C. Olson, Matthew C. Franklin*

The interleukin-6 (IL-6) family cytokines signal through gp130 receptor homodimerization or heterodimerization with a second signaling receptor and play crucial roles in various cellular processes. We determined cryo–electron microscopy structures of five signaling complexes of this family, containing full receptor ectodomains bound to their respective ligands ciliary neurotrophic factor, cardiotrophin-like cytokine factor 1 (CLCF1), leukemia inhibitory factor, IL-27, and IL-6. Our structures collectively reveal similarities and differences in the assembly of these complexes. The acute bends at both signaling receptors in all complexes bring the membrane-proximal domains to a ~30 angstrom range but with distinct distances and orientations. We also reveal how CLCF1 engages its secretion chaperone cytokine receptor–like factor 1. Our data provide valuable insights for therapeutically targeting gp130-mediated signaling.

INTRODUCTION

Glycoprotein 130 (gp130) is a signaling receptor shared by interleukin-6 (IL-6) family cytokines (or gp130 family cytokines), including IL-6, ciliary neurotrophic factor (CNTF), cardiotrophin-like cytokine factor 1 (CLCF1), leukemia inhibitory factor (LIF), oncostatin M (OSM), cardiotrophin-1 (CT-1), IL-11, IL-27, IL-35, and IL-39 (*1*). These cytokines share a canonical four-helix bundle structure in which four major helices (termed helices A to D) are linked by three loops (termed AB, BC, and CD loops), as well as three conserved receptor binding epitopes (termed sites 1 to 3). Signals induced by these cytokines play critical and diverse roles in the regulation of various cellular processes, including inflammatory and immune responses, embryonic development, neuronal and liver regeneration, and hematopoiesis, while dysregulation of these signals leads to a variety of diseases and cancers (*2*). IL-6 and IL-11 signal through gp130 homodimerization, while other cytokines require another "tall" signaling receptor, such as LIF receptor (LIFR) or IL-27 receptor subunit alpha (IL-27Rα), which forms a heterodimer with gp130 for signal transduction (*1*). The extracellular domains (ECDs) of gp130 include an N-terminal immunoglobulin (Ig)–like domain (D1), a cytokine-binding homology region (CHR, D2D3), and three membrane-proximal fibronectin type III domains (FNIII, D4 to D6). LIFR and IL-27Rα ECDs share a similar domain arrangement at the C terminus to gp130, but LIFR has an additional CHR preceding the Ig-like domain, while IL-27Rα does not have the N-terminal Ig-like domain.

IL-6 forms a symmetric 2:2:2 signaling complex with gp130 and IL-6 receptor subunit alpha (IL-6Rα) (*3*). CNTF binds to CNTF receptor subunit alpha (CNTFRα) first and then assembles into a 1:1:1:1 quaternary signaling complex with gp130 and LIFR (*4*, *5*). CLCF1 was also found to interact with CNTFRα and signal via the gp130-LIFR heterodimer analogous to CNTF, and cytokine receptor–like factor 1 (CRLF1) was shown to chaperone the secretion of CLCF1 (*6*). LIF forms a 1:1:1 tripartite complex with gp130 and LIFR, and the signal transduction does not require a nonsignaling alpha receptor (*7*). IL-27 is a heterodimeric cytokine of p28 and Epstein-Barr virus–induced gene 3 (EBI3) and signals through gp130 and IL-27Rα by forming a 1:1:1:1 quaternary complex (*8*).

It has been proposed that the membrane-proximal domains of the two signaling receptors are brought into close proximity upon assembly of the gp130 family cytokine signaling complexes, which allows transphosphorylation of Janus kinases (JAKs) bound to the intracellular domains (ICDs) of the two receptors (*9*, *10*). Specific cytoplasmic tyrosine–containing motifs in these receptors are phosphorylated by JAKs and consequently serve as docking sites for recruitment and activation of the signal transducers and activators of transcription (STATs), which eventually translocate to the nucleus to regulate gene expression (*11*).

Despite the importance of the gp130 family cytokine signaling complexes in diverse cellular processes, the structures of these complexes are not well characterized because of their high flexibility and instability. The IL-6 signaling complex is best characterized with a 3.65-Å crystal structure of the assembly core region and a low-resolution negative stain electron microscopy (EM) map of the complex with full gp130 ectodomains (*3*, *10*). A low-resolution negative stain EM map was also reported for the CNTF signaling complex, but the assembly details are not clear (*9*). Two other studies have revealed how human gp130 D2D3 and mouse LIFR (mLIFR) D1 to D5 engage LIF (*7*, *12*). In addition, two cryo-EM structures of the IL-27 signaling complex assembly core region were reported most recently (*13*, *14*). However, the overall architectures of the LIF and IL-27 signaling complexes remain unknown. Moreover, there is no structural information for the CLCF1 signaling complexes, and how CLCF1 engages its secretion chaperone CRLF1 is elusive.

We have determined cryo-EM structures of the signaling complexes for CNTF, CLCF1, LIF, and IL-27 at sub–4-Å resolution using full ectodomains of both signaling receptors in these complexes. We have also obtained a 3.22-Å cryo-EM structure for the IL-6 signaling complex using detergent-solubilized gp130

Regeneron Pharmaceuticals Inc., Tarrytown, NY 10591, USA.
*Corresponding author. Email: yi.zhou@regeneron.com (Y.Z.); matthew.franklin@regeneron.com (M.C.F.)

containing transmembrane (TM) domain and intracellular Box1/Box2 motifs where JAKs bind. Our structures reveal that gp130 serves as a central receptor by engaging site 2 of CNTF, CLCF1, LIF, and IL-6, and site 3 of IL-27 and IL-6. The acute bends at both signaling receptors in these complexes bring the juxtamembrane domains to a ~30-Å range but with distinct distances and orientations, which might determine biological specificities of the cytokines. In addition, we have solved a 3.40-Å cryo-EM structure of the CRLF1-CLCF1-CNTFRα complex, which exhibits an unexpected 2:2:2 stoichiometry. CLCF1 sites 2 and 3 are engaged by two CRLF1 molecules analogous to how they are engaged by gp130 and LIFR in the CLCF1 signaling complex. Our results have provided valuable insights into the assembly and signaling mechanisms of gp130 family cytokine–receptor complexes.

RESULTS

Structural characterization of the CNTF, CLCF1, and LIF signaling complexes

Using cryo-EM, we obtained structures of the human CNTF, CLCF1, and LIF signaling complexes, which exhibit similar structural architectures and assembly mechanisms (Figs. 1 and 2). In these complexes, sites 2 and 3 of the ligands bind to gp130 and LIFR, respectively, while site 1 is occupied by CNTFRα or left empty. Residue numbering of all proteins described here is based on their UniProt sequences.

Cryo-EM structure of the CNTF signaling complex

We reconstituted the quaternary CNTF signaling complex using full ectodomains of gp130 and LIFR, and a fusion protein of CNTFRα and CNTF linked by a flexible linker (fig. S1). The complex was characterized by single-particle cryo-EM, generating a density map with a global resolution of 3.03 Å (fig. S2, A to E). This map has well-resolved density around the interaction core region, including CNTF, CNTFRα D2D3, gp130 D2 to D5, and LIFR D2 to D5, permitting manual model building and real-space refinement of this region. Because of the flexible nature of the receptors, the local resolution at the distal ends of the receptors is lower. The membrane-proximal FNIII domains (D6 to D8) of LIFR have fragmented density, likely due to high heterogeneity induced by the flexibility of this region. A subset of particles was further identified by heterogeneous refinement, yielding another map with lower global resolution (3.37 Å) but improved density for LIFR D6 to D8 (Fig. 1A and fig. S2, F and G). The second map was used for placement and rigid-body fitting of models for the receptor distal domains, which were derived from published structures [gp130 D1 (*3*), gp130 D6 (*2*), and LIFR D1 (*9*)] or predicted by AlphaFold (LIFR D6 to D8) (*15*). In addition, to help build the model for CNTFRα D1, we determined a 2.93-Å cryo-EM structure of CNTFRα full ectodomain with the help of two antibody Fab fragments bound to CNTFRα D1 and D2, respectively (fig. S3). The CNTFRα D1 model derived from this structure was also fitted into the 3.37-Å CNTF signaling complex map as a rigid body. Combining all of this, we generated a complete model of the CNTF signaling complex with full ECDs (Fig. 1B). Intriguingly, the acute bends of gp130 at D4D5 and LIFR at D6D7 bring the bottom centers of the receptor juxtamembrane domains to ~24 Å apart (Fig. 1C).

CNTF site 1 is occupied by CNTFRα, similar to how IL-6 is engaged by IL-6Rα (*3*). CNTFRα D2D3 adopts an elbow-like conformation and holds CNTF in its hinge region by interacting with CNTF helices A and D and AB loop (Figs. 1B and 2A). The interface is enriched with charged residues, including CNTFRα^{D261,E286} and CNTF^{R25,H174,R177}, which mediate a network of hydrogen bonds and salt bridge interactions. The interface is centered around CNTFRα^{F172}, which is surrounded by W64, V170, R171, and H174 of CNTF. The C terminus of the CNTF AB loop is held in position through hydrophobic interactions between CNTF^{W64} and CNTFRα^{F172,F238}. Notably, F172 and E286 in CNTFRα are two residues that contribute the two highest buried surface areas (134 and 107 Å^2, respectively), consistent with their key roles in ligand binding (*16*). The importance of CNTF^{W64} in the interaction is also supported by a previous mutagenesis study (*17*).

On the other side of site 1, CNTF helices A and C are captured by the elbow region of gp130 CHR (D2D3), forming the site 2a interface (Figs. 1B and 2B). Similar to the way gp130 engages LIF (*12*) and IL-6 (*3*), gp130^{F191} contributes the largest fraction of buried surface area (119 Å^2) at the gp130-CNTF interface by inserting into a hydrophobic pocket formed by W22, L23, and the hydrophobic portions of R19 and K26 on helix A of CNTF. CNTF^{R19} is also coordinated by gp130^{D215} to form hydrogen bond and salt bridge at the center of the interface. CNTF helix C is held in position by gp130^{W164} packing against the middle of the helix. While the interactions are predominantly mediated by gp130 D2, V252 from D3 interacts with W22 and K26 at the middle of CNTF helix A, which likely improves the binding.

CNTFRα D3 leans against gp130 D3 to make a "stem-stem" site 2b interaction, contributing an additional 1386 Å^2 buried surface area to the composite site 2 (Fig. 1B), which likely increases the overall binding affinity. Consistent with this, CNTF is not able to initiate signaling in the absence of CNTFRα (*5*). The site 2b interface is dominated by hydrophilic interactions and centered around CNTFRα^{D269}, which pairs with gp130^{R281,T285} (Fig. 2C). A hydrophobic patch of CNTFRα residues (I250, L251, and Y271) further anchors the distal end of its D3 to gp130 by engaging L236 and I239 of gp130.

LIFR contacts the posterior end of the CNTF four-helix bundle, including the N terminus of the AB loop and helix D, the C terminus of helix B, and the short BC loop, to form the site 3 interface where 27 LIFR residues and 25 CNTF residues together bury a total of 1525 Å^2 surface area (Figs. 1B and 2D). The interactions are predominantly mediated by the LIFR D3 (Ig) domain, with the N-terminal loop of D4 serving as a supporting binding site. Two residues at the N terminus of CNTF helix D, F152 and K155, play crucial roles in the binding, with additional interactions mediated by the packing of hydrophobic patches at the CNTF AB and BC loops against LIFR D3 and D4, respectively. The aromatic ring of CNTF^{F152} makes a π stacking against the peptide bond of LIFR^{G324}, which is sitting at the bottom of a hydrophobic cavity formed by N313, V315, I322, and V326 of LIFR. CNTF^{K155} is coordinated by LIFR^{S310,N313} to form hydrogen bonds. Supporting these observations, CNTF F152 and K155 have been shown to be essential for binding to LIFR in a mutagenesis study (*18*). Notably, CNTF F152 and K155 form an F*XX*K motif that is evolutionarily conserved among other IL-6 family cytokines that bind to LIFR. The equivalent residues in LIF and CLCF1 are F178 and K181. It was reported that F178 and K181 in human LIF (hLIF) engage mLIFR in a highly similar manner (*7*).

Cryo-EM structure of the CLCF1 signaling complex

CLCF1 signals through the same receptors as CNTF. Using full ectodomains of gp130 and LIFR and a fusion protein of CNTFRα and CLCF1 linked by a flexible linker (fig. S1), we obtained a 3.90-Å cryo-EM map of the CLCF1 quaternary signaling complex, which has well-resolved density around the interaction core region, including CLCF1, CNTFRα D2D3, gp130 D2 to D5, and LIFR D2 to D5, permitting manual model building and real-space refinement (Fig. 1, D and E, and fig. S4). Density at the receptor distal ends (gp130 D1 and D6, LIFR D1 and D6 to D8, and CNTFRα D1) was sufficient for placing models of these domains as rigid bodies as with the CNTF complex. The bottom centers of LIFR and gp130 juxtamembrane domains are positioned ~22 Å apart (Fig. 1F), comparable to that seen in the CNTF complex.

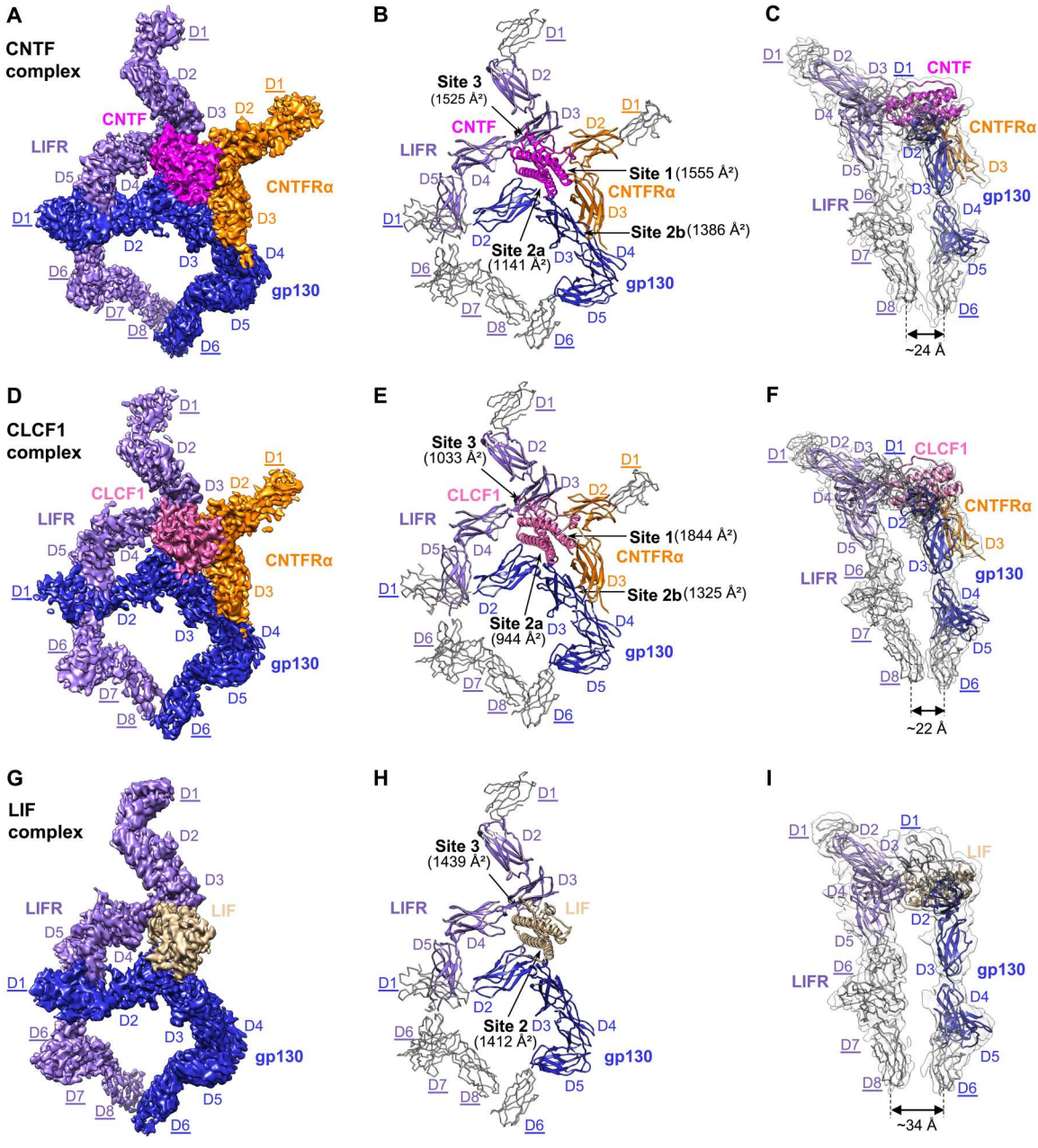

Fig. 1. Cryo-EM structures of the CNTF complex, CLCF1 complex, and LIF complex. (**A** to **C**) The CNTF signaling complex is shown in three representations: colored cryo-EM density map (A), cartoon representation of the model containing full ECDs (B), and side view of the model in the transparent EM density map, low-pass filtered to better show density in the peripheral domains (C). (**D** to **F**) The CLCF1 signaling complex is shown similarly to (A) to (C). (**G** to **I**) The LIF signaling complex is shown similarly to (A) to (C). Models for receptor peripheral domains (gp130 D1 and D6, LIFR D1 and D6 to D8, and CNTFRα D1) that were only rigid-body fitted into the density to show the positions of these domains are colored gray and depicted as C-alpha ribbon traces. The corresponding labels are underlined [these domains are not included in Protein Data Bank (PDB) depositions]. The interaction interfaces with corresponding buried surface areas calculated by PDBePISA are indicated by arrows in (B), (E), and (H). Approximate distances between the bottom centers of LIFR and gp130 juxtamembrane domains in each complex are shown in (C), (F), and (I).

Similar to CNTF, CLCF1 site 1 is captured by the elbow region of CNTFRα (Fig. 1E). CNTFRα^{F172} also serves as the anchor point of the CNTFRα-CLCF1 interface by engaging T193, W196, R197, and K200 of CLCF1 (Fig. 2E). Multiple electrostatic interactions are observed between positively charged CLCF1 residues (R48, R95, and K200) and negatively charged CNTFRα residues (D234, D284, and E286). Notably, each of the key CNTFRα residues, including F172, T174, and E286, contributes substantial binding interactions to both CNTF and CLCF1 (Fig. 2I). It has been reported that W94, R197, and D201 of CLCF1 are critical for binding to CNTFRα (*19*). A CLCF1^{R197L} mutation allele was also identified in patients, and the mutated protein failed to bind to CNTFRα (*20*). These observations align well with our structure, which suggests that W94 plays an important role in packing the C terminus of the CLCF1 AB loop against CNTFRα through a hydrophobic interaction with CNTFRα F238 (Fig. 2E). The hydrophobic portion of CLCF1^{R197} also directly engages CNTFRα by leaning against CNTFRα^{F172}. CLCF1^{D201} does not directly contact CNTFRα; however, it forms a hydrogen bond with CLCF1^{W94} and likely holds W94 in position to interact with CNTFRα.

Like CNTF, CLCF1 binds to gp130 D2D3 to form the site 2a interface (Fig. 1E). Key gp130 residues engaging CNTF maintain their roles in the CLCF1 complex, with F191 engaging K42, D45, L46, and Y49 of CLCF1 helix A; D215 forming a hydrogen bond with CLCF1^{K42} at the center of the interface; and W164 capturing the middle portion of CLCF1 helix C (Fig. 2F).

The CLCF1 complex shares the same site 2b interface as the CNTF complex where CNTFRα D3 is docked into a wide cavity of gp130 D3 to stabilize the binding of CLCF1 to gp130 (Figs. 1E and 2G). Similarly, site 2b (1325 Å^2) has a larger buried surface area than site 2a (944 Å^2) in the CLCF1 complex and greatly increases interactions at the composite site 2, which may explain why CNTFRα is indispensable for CLCF1 signaling (*6*).

CLCF1 also binds to LIFR D3 to form the site 3 interface. Notably, 72% of CLCF1 residues contributing to the packing of this interface are nonpolar, which is much higher than the percentage of nonpolar CNTF residues at the CNTF-LIFR interface (44%). Despite this difference in residue polarity, LIFR captures CLCF1 in a similar manner to how it engages CNTF. Like F152 and K155 of CNTF, the two conserved CLCF1 residues F178 and K181 also serve as key anchor points engaging LIFR residues (S310, N313, V315, I322, G324, and V326) (Fig. 2H), consistent with previous mutagenesis studies (*19*, *21*). CLCF1 helix B does not make extensive contacts with the N-terminal loop of LIFR D4 as CNTF helix B does, because CLCF1 helix B is slightly shorter than CNTF helix B at the C terminus. In addition, fewer hydrogen bonds are formed at the CLCF1-LIFR interface compared with the CNTF-LIFR interface due to the lower percentage of polar/charged residues at CLCF1 site 3. These two factors together may have led to a significantly lower buried surface area of the CLCF1-LIFR interface (1033 Å^2) than the CNTF-LIFR interface (1525 Å^2).

Cryo-EM structure of the LIF signaling complex

LIF signals via gp130 and LIFR in the absence of a nonsignaling alpha receptor. The overall architecture of this tripartite signaling complex remains unknown. We therefore reconstituted the complex using full ectodomains of gp130 and LIFR (fig. S1) and obtained a 3.54-Å cryo-EM map (fig. S5). As with the CNTF and CLCF1 complexes, this map's higher resolution around the interaction core region (LIF, gp130 D2 to D5, and LIFR D2 to D5) permitted full model building and refinement, while the density at the distal domains of the receptors (gp130 D1 and D6, LIFR D1 and D6 to D8) was sufficient for domain placement as rigid bodies (Fig. 1, G to I).

The gp130-LIF interface has a larger buried surface area (1412 Å^2) than the gp130-CNTF and gp130-CLCF1 interfaces (Fig. 1), which is mostly caused by gp130 engaging LIF N-terminal extension (residues 34 to 42) preceding helix A (Fig. 2J). Consistent with the crystal structure of gp130 D2D3 in complex with LIF (*12*), the LIF N-terminal extension serves as a "doorstop" to hold gp130 in position and creates additional interaction interface, which might be the reason why LIF does not need a nonsignaling alpha receptor. Of the 21 LIF residues forming the contacting surface, R37 and H38 from the N-terminal extension contribute the two highest fractions of buried surface area through electrostatic interactions with gp130^{E163,E195}. In contrast, similar N-terminal extension with a rigid conformation is not seen in CNTF or CLCF1. W164 and F191 of gp130 also engage LIF analogous to how they interact with CNTF and CLCF1. While gp130 largely covers the middle region of helices A and C of CNTF and CLCF1, it is positioned toward the N terminus of LIF helix A, leading to an increased distance between the bottom centers of gp130 D6 and LIFR D8 in the LIF complex (~34 Å) (Fig. 1I).

Similar to CNTF and CLCF1, LIF also engages LIFR via the conserved F*XXK* motif at site 3 (Fig. 2K). The way hLIFR residues (S310, N313, V315, I322, G324, and V326) interact with hLIF^{F178,K181} is also observed in the hLIF/mLIFR D1 to D5 complex crystal structure (*7*), consistent with the cross-reactivity of hLIF with both hLIFR and mLIFR. LIF is primarily docked onto the saddle-shaped LIFR D3 through its helix D and AB loop, with additional contacts made between the LIF BC loop and the N-terminal loop of LIFR D4. In addition to the key residues F178 and K181 in LIF helix D, P73 and K80 in the AB loop also make extensive contacts with LIFR. Consistent with our structure, a previous alanine substitution study has proven the importance of these LIF residues in LIFR binding (*22*).

Structural characterization of the CRLF1-CLCF1-CNTFRα complex

The secretion of CLCF1 was shown to require its chaperone CRLF1 (*6*). However, how CRLF1 engages CLCF1 is unclear. It was reported that CRLF1 forms a tripartite complex with CLCF1 and CNTFRα and promotes CLCF1 binding to CNTFRα (*23*). We reconstituted the human CRLF1-CLCF1-CNTFRα complex and obtained a 3.40-Å cryo-EM structure (Fig. 3 and figs. S1 and S6). Unexpectedly, the complex is a 2:2:2 hexamer with twofold symmetry (Fig. 3, A and B). The two CNTFRα molecules bind to site 1 of the two CLCF1 ligands without contacting CRLF1, indicating that CNTFRα may not be essential for CLCF1-mediated CRLF1 dimerization. Consistent with this, we solved a 3.45-Å cryo-EM structure of the CRLF1-CLCF1 complex, showing that CLCF1 and CRLF1 are able to form a symmetric 2:2 tetramer in the absence of CNTFRα (fig. S7). The two CRLF1 molecules captures two CLCF1 ligands analogous to how two gp130 receptors engage two viral IL-6 (vIL-6) ligands (fig. S7, D and E) (*24*).

The elbow region of CRLF1 D2D3 engages CLCF1 site 2 mimicking the interactions between gp130 D2D3 and CLCF1 (Fig. 3C). CRLF1 contacts a total of 24 CLCF1 residues, including all 13

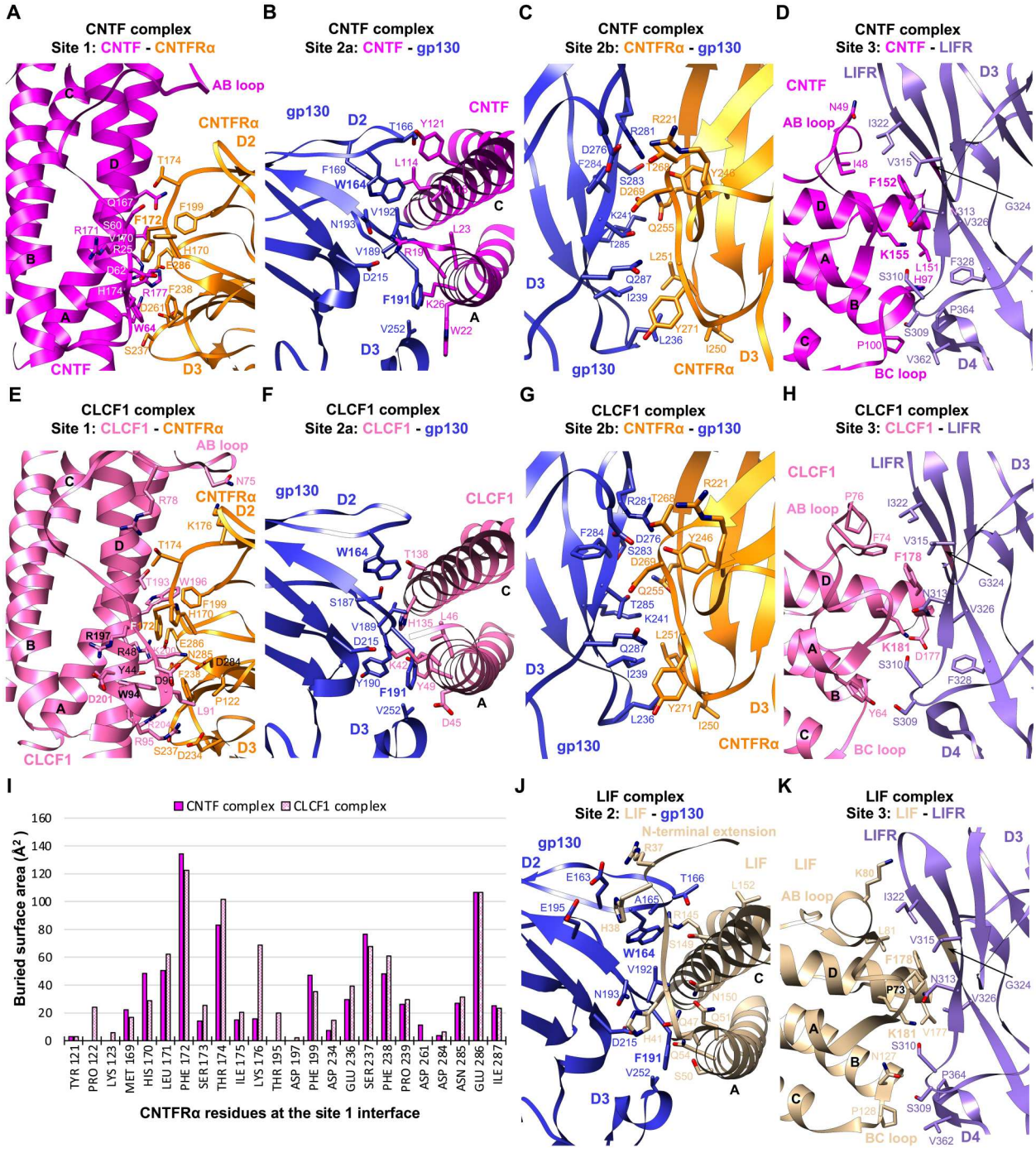

Fig. 2. Interaction interfaces of the CNTF complex, CLCF1 complex, and LIF complex. (**A** to **D**) The binding interfaces of the CNTF complex at site 1 (A), site 2a (B), site 2b (C), and site 3 (D), as indicated in Fig. 1B, are shown in cartoon form, with residues involved in binding shown in stick representation. All-atom real space–refined model of the CNTF complex interaction core region (CNTF, CNTFRα D2D3, gp130 D2 to D5, and LIFR D2 to D5) was used for the analysis. (**E** to **H**) The CLCF1 complex binding interfaces at site 1 (E), site 2a (F), site 2b (G), and site 3 (H), as indicated in Fig. 1E, are shown in the same representation as (A) to (D). All-atom real space–refined model of the CLCF1 complex interaction core region (CLCF1, CNTFRα D2D3, gp130 D2 to D5, and LIFR D2 to D5) was used for the analysis. (**I**) Histogram of buried surface area for CNTFRα residues at the site 1 interface in the CNTF and CLCF1 signaling complexes. (**J** and **K**) Details of the LIF complex binding interfaces at site 2 (J) and site 3 (K) as indicated in Fig. 1H. All-atom real space–refined model of the LIF complex interaction core region (LIF, gp130 D2 to D5, and LIFR D2 to D5) was used for the analysis.

residues that are covered by gp130 (Fig. 3F). Therefore, the CRLF1-CLCF1 interface has a much larger buried surface area (1480 Å^2) than the gp130-CLCF1 interface (944 Å^2). Notably, the three gp130 residues crucial for engaging CLCF1, W164, F191, and D215 all have equivalents in CRLF1 at similar locations, i.e., W177, F204, and D228, respectively. These CRLF1 residues interact with CLCF1 analogous to the corresponding gp130 residues. While F204 is inserted into a cavity formed by CLCF1 K42, D45, L46, and Y49 at helix A, W177 packs against helix C and D228 pairs with K42 of CLCF1. The involvement of several other aromatic residues of CRLF1 in the interactions, including Y178, F266, and Y319, further stabilizes the binding. Unlike gp130 D3, which only contributes 9.8% of the buried surface area to the gp130-CLCF1 interface (Fig. 2F), CRLF1 D3 contributes a much larger fraction of buried surface area (24.5%) to the site 2 CRLF1-CLCF1 interface (Fig. 3C).

Furthermore, the way LIFR D3 captures CLCF1 site 3 is copied by D1 of another CRLF1 molecule, CRLF1′, in the CRLF1-CLCF1-CNTFRα complex (Fig. 3D). The F*XXX*K motif of CLCF1 also dominates the binding to CRLF1′. CLCF1 F178 is stacked against CRLF1′ G126′ and is surrounded by N113′, V115′, I123′, and C128′ of CRLF1′, while CLCF1 K181 coordinates with S110′, N113′, and C128′ of CRLF1′ to form hydrogen bonds. In addition, key CLCF1 site 3 residues are all shared by CRLF1′ and LIFR for binding to this site (Fig. 3G). Consistent with our structure, the critical roles of CLCF1 F178 and K181 in engaging CRLF1′ have been supported by alanine substitutions (*19*).

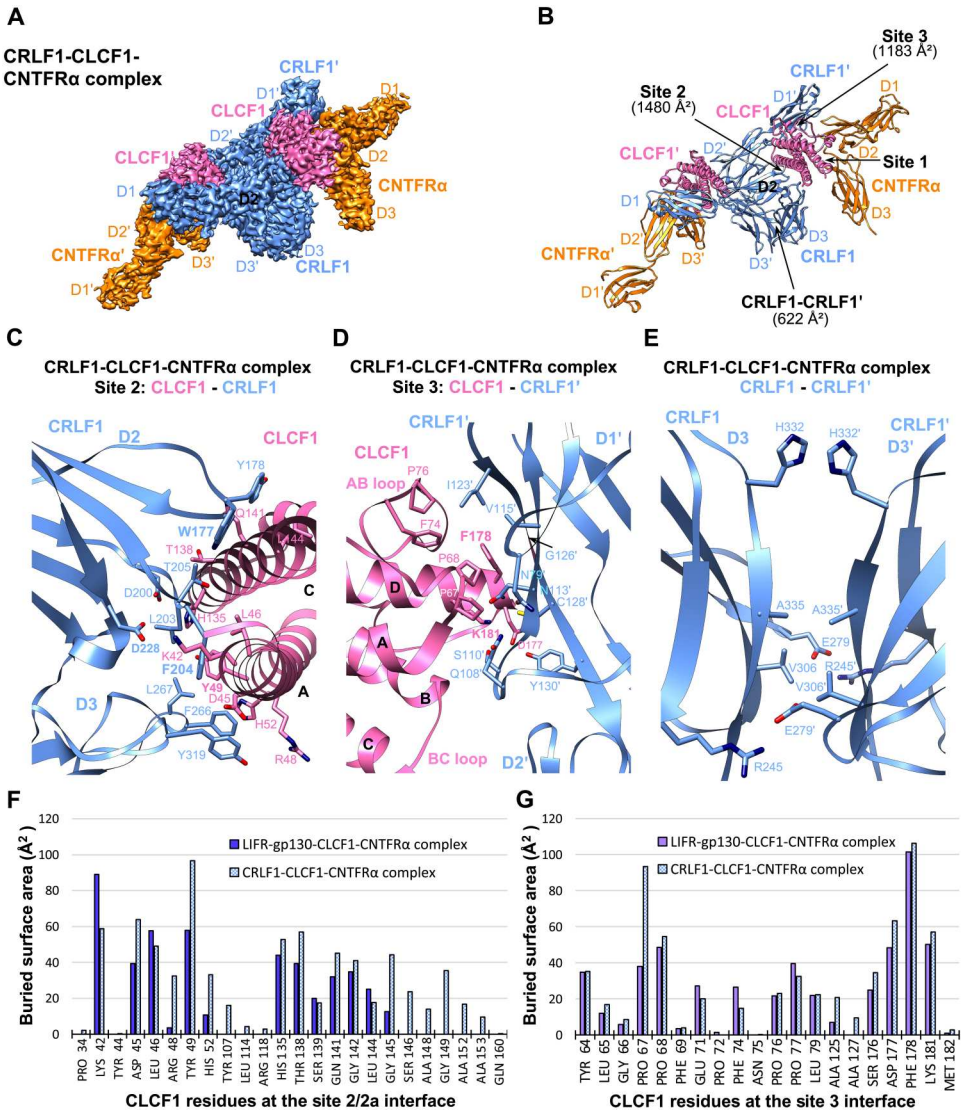

Fig. 3. Cryo-EM structure of the CRLF1-CLCF1-CNTFRα complex. (**A**) Cryo-EM density map of the CRLF1-CLCF1-CNTFRα complex. The two sets of molecules in the hexameric complex are annotated as CRLF1, CLCF1, CNTFRα, CRLF1′, CLCF1′, and CNTFRα′. (**B**) Cartoon representation of the CRLF1-CLCF1-CNTFRα complex. Site 2 and site 3 interfaces and the CRLF1 dimer interface with corresponding buried surface areas calculated by PDBePISA are indicated by arrows. (**C** to **E**) Details of binding interfaces at site 2 (C), site 3 (D), and the CRLF1 dimer interface (E), as indicated in (B). (**F** and **G**) Histograms of buried surface area for CLCF1 residues at site 2/2a (F) and site 3 (G) interfaces in the LIFR-gp130-CLCF1-CNTFRα complex (CLCF1 signaling complex) and the CRLF1-CLCF1-CNTFRα complex.

The two CRLF1 molecules also directly contact each other at their D3 domains (Fig. 3E). While R245 of one CRLF1 couples to E279 of another CRLF1 to form hydrogen bonds and salt bridges, H332, A335, and V306 from one molecule pack against the same corresponding residues from another molecule to hold both CRLF1 D3 domains together. However, this interface has a small buried surface area (622 Å^2) with a limited number of residues involved in the interactions.

Structural characterization of the IL-27 and IL-6 signaling complexes

To make a comprehensive analysis for the assembly of the gp130 family cytokine receptor complexes, we further determined cryo-EM structures of the human IL-27 and IL-6 signaling complexes, which share similar "sites 1 to 3" interactions with site 3 of both ligands engaging gp130 (Figs. 4 and 5).

Cryo-EM structure of the IL-27 signaling complex

IL-27, a heterodimeric cytokine composed of p28 and a soluble receptor EBI3, signals via IL-27Rα and gp130. Unlike CNTF, CLCF1, and LIF, which all bind to gp130 D2D3 at site 2, p28 engages gp130 D1 at site 3. Using full ectodomains of gp130 and IL-27Rα and an EBI3-p28 fusion protein linked by a flexible linker (fig. S1), we obtained a 4.14-Å cryo-EM map of the IL-27 quaternary signaling complex that has well-resolved density for domain placement and rigid-body refinement (Fig. 4A and fig. S8, A to D). We further ran a focused refinement around the interaction core region, including p28, EBI3, IL-27Rα D1D2, and gp130 D1 to D3, and obtained a 3.81-Å map that was used for manual model building and real-space refinement of this region (fig. S8, E to G). This model, together with a published structure of gp130 D4 to D6 (*2*) and a mode of IL-27Rα D3 to D5 predicted by AlphaFold, was rigid-body fitted into the 4.14-Å full map to generate a more complete model for the IL-27 complex (Fig. 4B). Intriguingly, an acute bend analogous to that found in gp130 and LIFR also exists between D3 and D4 of IL-27Rα. This bend, together with the bend of gp130 at D4D5, brings the receptor juxtamembrane domains into close proximity (~19 Å between the bottom centers of gp130 D6 and IL-27Rα D5) (Fig. 4C).

Our structure agrees well with two recently published cryo-EM structures of the IL-27 signaling complex interaction core region (*13*, *14*). EBI3 makes a broad contact with p28 helices A and D and the AB loop at the site 1 interface to bury a surface area of up to 2354 Å^2 (Figs. 4B and 5A). A network of hydrogen bonds and salt bridges mediate the interactions, with extensive hydrophobic interactions further stabilizing the binding. The interface is centered around E211 and R219 of p28, which form hydrogen bonds with Y211 and T209 of EBI3, respectively. EBI3 F97, similar to the evolutionarily conserved CNTFRα residue F172 in the CNTF and CLCF1 complexes, contributes a large buried surface area (152

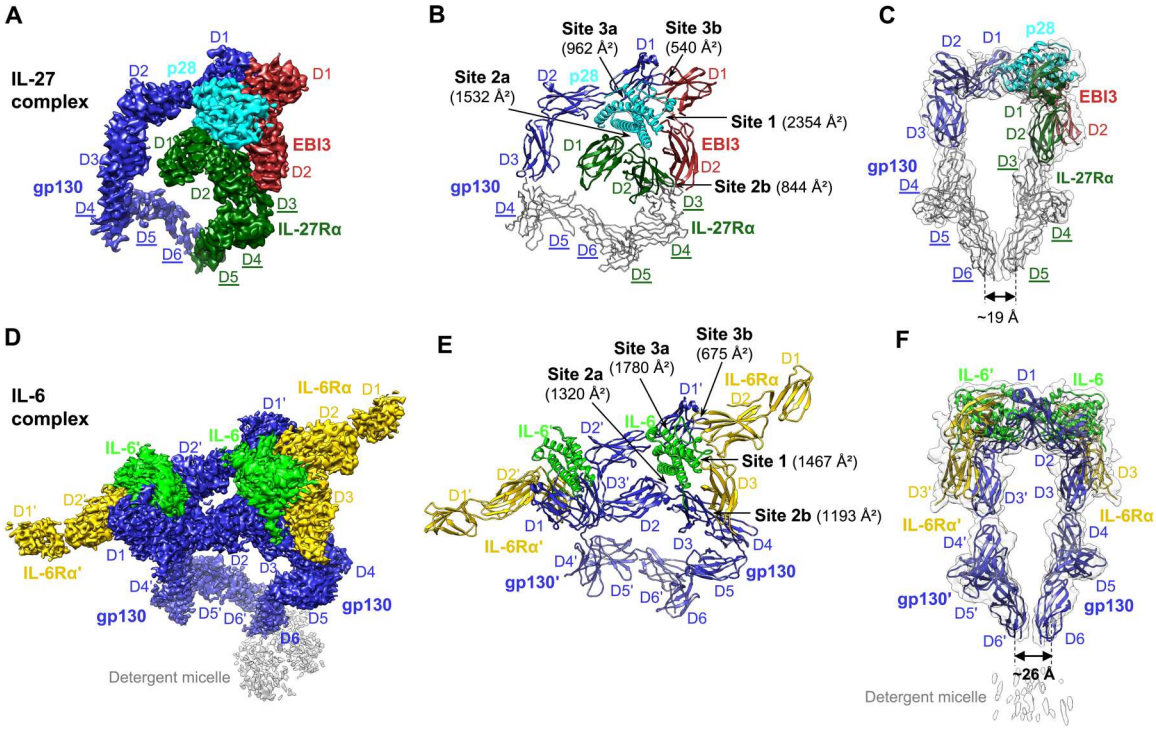

Fig. 4. Cryo-EM structures of the IL-27 complex and detergent-solubilized IL-6 complex. (**A** to **C**) The IL-27 signaling complex is shown as a colored cryo-EM density map (A), a cartoon representation of the model (B), and a side view of the model in transparent low-pass–filtered density map (C). Models for receptor peripheral domains (gp130 D4 to D6 and IL-27Rα D3 to D5) that were only rigid-body fitted into the density to show the positions of these domains are colored gray and depicted as C-alpha ribbon traces. The corresponding labels are underlined (these domains are not included in PDB depositions). (**D** to **F**) Cryo-EM density map (D), cartoon representation (E), and side view of the model in transparent low-pass–filtered density map (F) of the IL-6 complex in detergent. The two sets of molecules in the hexameric complex are annotated as gp130, IL-6, IL-6Rα, gp130′, IL-6′, and IL-6Rα′. The interaction interfaces with corresponding buried surface areas calculated by PDBePISA are indicated by arrows in (B) and (E). The distance between the bottom centers of the receptor juxtamembrane domains in each complex is estimated and shown in (C) and (F).

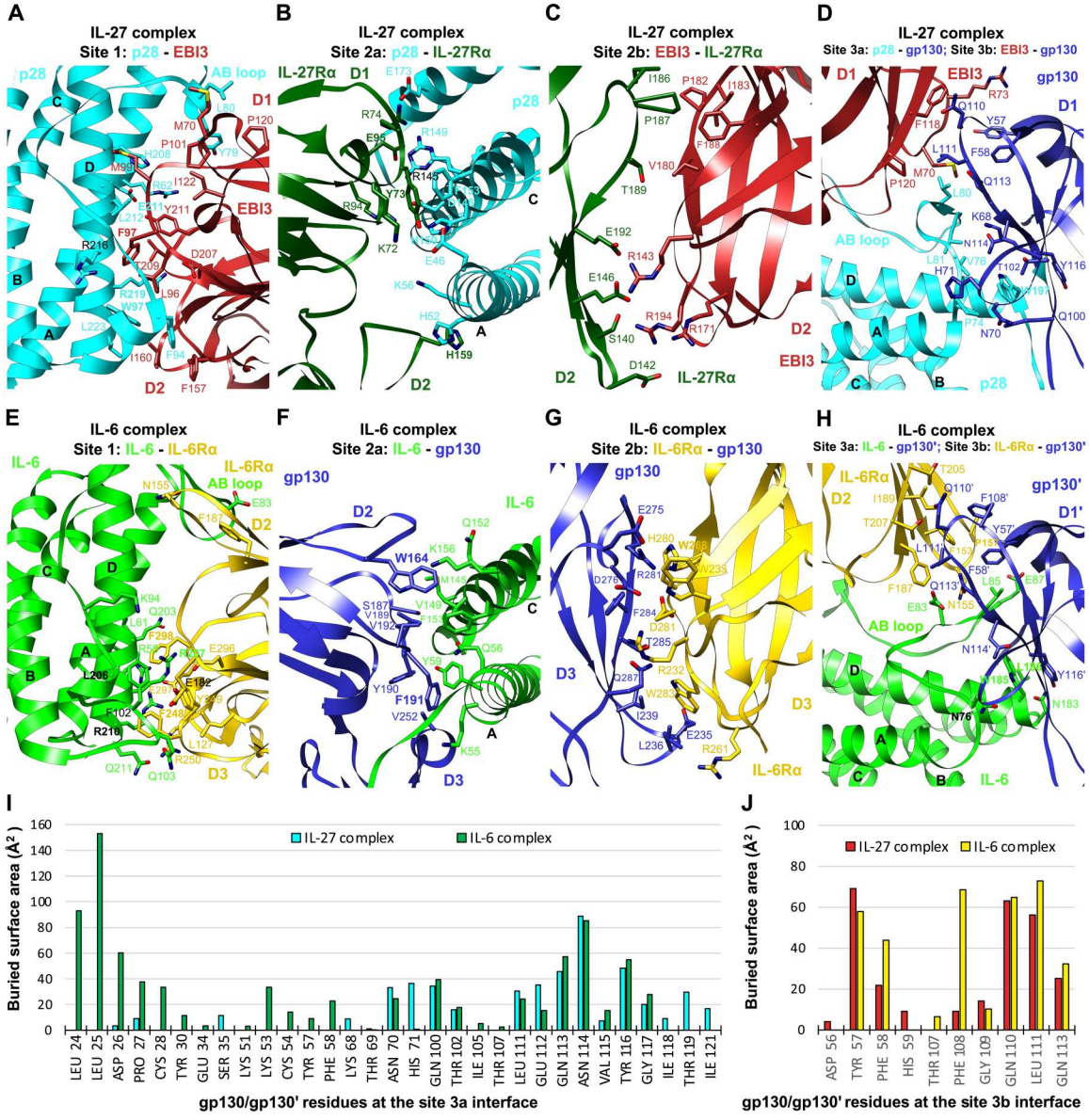

Fig. 5. Interaction interfaces of the IL-27 complex and IL-6 complex. (**A** to **D**) Details of binding interfaces of the IL-27 complex at sites 1, 2a, 2b, and 3a/3b, as indicated in Fig. 4B. All-atom real space–refined model of the IL-27 complex interaction core region (IL-27 p28, EBI3, IL-27Rα D1D2, and gp130 D1 to D3) was used for the analysis. (**E** to **H**) Details of binding interfaces of the IL-6 complex at sites 1, 2a, 2b, and 3a/3b, as indicated in Fig. 4E. (**I** and **J**) Histograms of buried surface area for gp130/gp130′ residues at site 3a (I) and site 3b (J) interfaces in the IL-27 complex and IL-6 complex.

Å^2) in the interface. Y79 and L80 at the N terminus of the p28 AB loop form a hydrophobic patch with M70, P101, P120, and I122 of EBI3. Another hydrophobic patch is formed at the C terminus of this loop, with F94, W97, and L223 of p28 engaging L96, F157, and I160 of EBI3. Consistent with our data, previous mutagenesis work has shown that EBI3^{F97} and p28^{W97} are both critical for IL-27 signaling (*25*). Notably, the equivalent residues of p28^{W97} at similar locations of CNTF and CLCF1, CNTF^{W64}, and CLCF1^{W94} are both crucial for interacting with CNTFRα (Fig. 2, A and E).

The p28 ligand binds to the hinge of IL-27Rα CHR (D1D2) at the site 2a interface (Fig. 5B), which is dominated by hydrogen bond and salt bridge interactions mediated by charged residues, including K72, R74, R94, and E95 of IL-27Rα and E46, K56, R145, D146, and E173 of p28. In addition, Y73 in D1 and H159 in D2 of IL-27Rα pack against p28^{H150,F153} at the C terminus of helix C, and p28^{K56,H52} at the middle of helix A, respectively. Notably, of the 18 IL-27Rα residues contacting p28, Y73, E95, and H159 make up ~40% of the buried surface area on the IL-27Rα side.

The "sandwiched" position of p28 between EBI3 and IL-27Rα is stabilized by the site 2b interactions mediated by IL-27Rα D2 and EBI3 D2 (Fig. 5C). This interface is enriched with negatively charged residues on IL-27Rα (D142, E146, and E192) and positively charged residues on EBI3 (R143, R171, and R194), which mediate electrostatic interactions. A hydrophobic patch of residues,

IL-27Rα^{I186,P187} and EBI3^{P182,I183,F188}, further improves the binding. The site 2b interface adds an 844-Å^2 buried surface area to site 2a, making a total buried surface area of 2376 Å^2 for the composite site 2 and leading to increased binding interactions, which might explain why p28 activity is EBI3 dependent (*26*).

Similar to the IL-6 complex (*3*), the IL-27 complex has a composite site 3 interface, including site 3a formed by gp130 Ig domain (D1) engaging p28 and site 3b formed by gp130 D1 contacting EBI3 D1 (Figs. 4B and 5D). Site 3a has a relatively limited buried surface area (962 Å^2) with W197 at the N terminus of p28 helix D packing against gp130^{Y116} to serve as a binding anchor. The aromatic residue W197, which is equivalent to a phenylalanine residue in the F*XXX*K motif of CNTF (F152), CLCF1 (F178), and LIF (F178), is evolutionarily conserved in IL-6 (W185) (*3*), vIL-6 (W166) (*24*), and IL-11 (W168) (*27*) and has been shown to be crucial for IL-27 signaling (*26*). A group of residues at the N terminus of the p28 AB loop (V76, L80, and L81) make additional hydrophobic contacts with gp130 D1. The site 3b interface is centered around EBI3^{F118} and has a small buried surface area (540 Å^2). The tip of gp130 D1 leans against the top side of EBI3 D1, and the interactions are largely hydrophobic.

Cryo-EM structure of the IL-6 signaling complex in detergent

We further characterized the IL-6 signaling complex in which the ligand binds to gp130 at both sites 2 and 3. With the goal of obtaining structural information for the TM domain, we purified gp130 with the TM region and cytoplasmic Box1/Box2 motifs and reconstituted the complex with IL-6Rα ectodomain and IL-6 in detergent (fig. S1). We obtained a 3.22-Å cryo-EM structure of this hexameric complex with twofold symmetry (Fig. 4, D and E, and fig. S9). Although a density corresponding to the detergent micelle is present, the TM helix and cytoplasmic region of gp130 are not resolved, and there is a ~15-Å gap between gp130 C-terminal density and the detergent micelle (fig. S9B), indicating some level of flexibility around gp130 TM domain, although the two TM helices are embedded inside the detergent micelle. The acute bend of gp130 at D4D5 brings the bottom centers of the two gp130 juxtamembrane domains to ~26 Å apart (Fig. 4F).

The overall architecture of the IL-6 signaling complex is very similar to that of the IL-11 signaling complex (*27*). The assembly of the IL-6 complex interaction core region agrees with the 3.65-Å crystal structure of gp130 D1 to D3/IL-6Rα D2D3/IL-6 complex (*3*). Briefly, the site 1 interface is dominated by IL-6Rα^{F248,F298} and IL-6^{R207,R210} through a network of hydrophobic and electrostatic interactions. The binding center at IL-6 site 1 is close to the C terminus of helix D, with IL-6Rα D3 contributing the majority (63.7%) of the buried surface area (Fig. 5E). In contrast, the site 1 binding centers of CNTF, CLCF1, and IL-27 p28 are all close to the middle of helix D, with the C-terminal domains of the corresponding alpha receptor (CNTFRα D3 and EBI3 D2) contributing less to the binding than the preceding domains (Figs. 2, A and E, and 5A). At site 2a of the IL-6 complex, W164 and F191 of gp130 engage IL-6 helices A and C, respectively, in a similar manner as they interact with CNTF, CLCF1, and LIF (Fig. 5F). The site 2b interface stabilizes the composite site 2 binding by introducing extra buried surface area, with gp130^{E235,D276,R281} and IL-6Rα^{R232,D281,W283} playing key roles (Fig. 5G). The site 3a interface is characterized by W185 on the C terminus of IL-6 helix D stacking with Y116′ on D1′ of the second gp130 receptor, gp130′ (Fig. 5H). Notably, the long AB loop of IL-6 is inserted into a broad cavity on the head of gp130′ D1′, and the N-terminal end of gp130′ extends in parallel with one side of the loop to mediate extensive interactions, both of which are not seen in the IL-27 complex (Fig. 5, D, H, and I). These differences lead to a much larger buried surface area at site 3a of the IL-6 complex (1780 Å^2) than that of the IL-27 complex (962 Å^2). Last, the site 3b interface of the IL-6 complex is made by the tip of gp130′ contacting the side of IL-6Rα D2 and is centered around IL-6Rα^{F153} (Fig. 5H). Key gp130′ residues that contact IL-6Rα at this interface also engage EBI3 in the IL-27 complex (Fig. 5J).

Structural similarities of cytokines and nonsignaling receptors in the gp130 family cytokine receptor complexes

We next compared seven gp130 family cytokines, including five characterized in this study, as well as OSM and IL-11, which are both well characterized structurally (*27*–*30*). Despite the low sequence identities of these cytokines (table S1), they all share a canonical four-helix bundle structure, where four major helices are linked by three loops (Fig. 6A). Notably, some key residues for receptor binding at sites 1 and 3 are conserved across different human cytokines, including CNTF^{W64}, CLCF1^{W94}, and IL-27 p28^{W97} at site 1; CNTF^{F152,K155}, CLCF1^{F178,K181}, LIF^{F178,K181}, and OSM^{F185,K188} at site 3 that engages LIFR; and IL-27 p28^{W197}, IL-6^{W185}, and IL-11^{W168} at site 3 that binds to gp130. Of the five gp130 family cytokine signaling complexes we examined, the LIF complex is the only one without a nonsignaling alpha receptor. Notably, the N-terminal extension of LIF preceding helix A is tethered to helix C by two disulfide bonds (C34 to C156 and C40 to C153) to adopt a rigid conformation to make extensive contacts with gp130 D2 (Fig. 2J). The additional buried surface area introduced by these contacts might serve to improve LIF site 2 affinity to gp130, which might explain why LIF does not require an alpha receptor for signaling. Another gp130 family cytokine, OSM, shares this alpha receptor independence to signal through gp130 and either LIFR or OSM receptor. OSM also has an N-terminal extension that is tethered to helix C by the C31 to C152 disulfide bond (*28*) and might also increase OSM site 2 affinity to gp130. In contrast, a similar conformation of a rigid N-terminal extension tethered to helix C by disulfide bonds is not observed in CNTF, CLCF1, IL-27 p28, or IL-6, which all require a nonsignaling receptor for signal transduction. Similar to the N-terminal extension of LIF, which makes additional contacts with gp130 D2 to increase the buried site 2 surface area, the nonsignaling receptors in the CNTF, CLCF1, IL-6, and IL-27 complexes all serve to increase the total buried surface area of the composite site 2 in these complexes by making extra site 2b contacts with the corresponding signaling receptor bound to site 2a (Figs. 1 and 4).

We further compared the structures of four nonsignaling receptors, including CNTFRα, IL-6Rα, and EBI3 characterized in our study, as well as IL-11Rα, which has been well studied by the Griffin group (*27*, *29*). No dramatic conformational changes of CNTFRα and IL-6Rα were observed upon ligand binding (Fig. 6, B and C). In addition, CNTFRα, IL-6Rα, IL-11Rα, and EBI3 adopt highly similar conformations at the elbow regions where the ligands bind (Fig. 6D). Notably, it has been reported that IL-6Rα could also serve as an alpha receptor for CNTF and IL-27 p28 instead of CNTFRα and EBI3, respectively (*31*, *32*), suggesting structural plasticity of the IL-6 family cytokines and receptors.

DISCUSSION

It has been very challenging to characterize the structures of the tall gp130 family cytokine receptors due to their common elongated geometry and resulting flexibility. To our knowledge, this paper presents the first high-resolution cryo-EM structure determination of the full ectodomains of this family of receptors, including gp130, LIFR, and IL-27Rα. Unexpectedly, in the complexes we characterized, gp130 and LIFR are both quite rigid overall, despite some degree of flexibility at the membrane-proximal regions (Fig. 7, A and B). There are no large conformational changes of the receptors upon cytokine binding as well. gp130 CHR (D2D3) engages CNTF, CLCF1, LIF, and IL-6 at site 2 in a highly similar manner, with 10 gp130 residues (W164, T166, H167, S187, V189, Y190, F191, V192, N193, and V252) being shared by all four cytokines and F191 playing a key role for binding (Fig. 7C). The ways in which LIFR engages CNTF, CLCF1, and LIF are even more conserved, with 17 LIFR residues being shared by the three cytokines (Fig. 7D). Important LIFR residues for binding include S310, N313, I322, and V326.

A common feature of the tall signaling receptors, gp130, LIFR, and IL-27Rα, is an acute bend (~80°) between the third to the last and the second to the last ECDs (i.e., gp130 D4D5, LIFR D6D7, and IL-27Rα D3D4), which appears to be a crucial geometry for signaling. The bends at the two signaling receptors in each of the signaling complexes we examined serve to bring the bottom centers of the receptor juxtamembrane domains to within about 30 Å. This is similar to the distances between the receptor juxtamembrane domains observed in multiple other cytokine receptor complexes that also activate the JAK/STAT pathway (fig. S7), including the Epo-EpoR complex (*33*), insulin-insulin receptor complex (*34*), and insulin-like growth factor 1 (IGF1)–IGF1 receptor (IGF1R) complex (*35*). Moreover, the ~30-Å distance is also comparable to the distance between the two membrane-proximal FERM-SH2 domains of dimeric JAK1 bound to Box1/Box2 motifs of a cytokine receptor on the intracellular side (*36*). These consistent observations suggest that bringing the two signaling receptor juxtamembrane domains to ~30 Å apart might be a prerequisite for activating the JAK/STAT pathway. Moreover, it has been shown that deletion of any of the gp130 membrane–proximal domains D4 to D6 leads to IL-6, IL-11, and LIF unresponsiveness (*37*, *38*). These domain deletions of gp130 will probably alter relative positions of the two signaling receptor juxtamembrane domains in the signaling complexes, placing the receptor TM helices in a geometry that is not favorable for JAK/STAT activation. It has been reported that changes in cytokine receptor dimer ECD orientation can alter signaling output (*39*).

The EM density of these juxtamembrane domains in most of our signaling complex maps does not permit detailed analysis of residue-residue interactions; however, we note that the modeled positions of the domains with the closest approach (e.g., in the IL-27 and CLCF1 complexes) will place residues in those domains close enough for direct contact, with Cα-Cα distances less than 6 Å. LIFR and gp130 do not directly interact with each other in the absence of ligand (*5*), suggesting that if there are indeed interactions between gp130 and LIFR juxtamembrane domains in the CNTF or CLCF1 complex, the interactions are likely dependent on ligand-induced receptor dimerization and should be quite weak. Notably, weak juxtamembrane domain interactions have been observed and experimentally proved to be crucial for the activation of several receptor tyrosine kinases, including KIT (*40*), vascular endothelial growth factor receptor-1 (VEGFR-1) (*41*), and insulin receptor (IR) (*34*). It is possible that the potential juxtamembrane domain contact in a few signaling complexes we characterized in this study is critical for signaling as well. Additional work is needed to verify this and figure out key residues involved in the possible weak interactions. Nevertheless, both human and mouse IL-27 signaling complexes were successfully reconstituted using membrane-proximal domain truncated receptors (gp130 D1 to D3 and IL-27Rα D1D2) (*13*, *14*), indicating that even if gp130 D6 directly contacts IL-27Rα D5 in the full IL-27 signaling complex as it appears in our cryo-EM map (Fig. 4C), this juxtamembrane interaction is not essential for the assembly of the complex.

The two gp130 juxtamembrane D6 domains in our IL-6 signaling complex are better resolved, presumably because the insertion of TM helices into the detergent micelle has restrained the flexibility of these domains. Consistent with the observation that no D6-D6 contacts are made in the gp130 crystal lattice (*2*), we do not see direct interactions between the gp130 juxtamembrane domains in the IL-6 signaling complex, which may explain why the presence of gp130 D4 to D6 did not increase gp130 binding affinity to IL-6 or IL-11 (*13*, *27*). In contrast, in the VEGF-A/VEGFR-1 complex, the presence of VEGFR-1 membrane-proximal D4 to D7 led to 20 times higher binding affinity of VEGFR-1 to the ligand (*41*). It is possible that the weak homotypic receptor-receptor interaction mediated by VEGFR-1 juxtamembrane domains could serve to stabilize the VEGF-A signaling complex (*41*), which is not the case for the IL-6 signaling complex since the two gp130 receptors in the complex do not contact each other at juxtamembrane domains.

The gp130 family cytokines all activate the JAK/STAT pathway, but how the signaling specificity is derived remains unclear. For example, it is not clear why IL-27 activates both STAT1 and STAT3, while IL-6 predominantly signals via STAT3 phosphorylation (*42*). Our data show that these cytokines do have variable loop conformations, especially at the N terminus of the AB loop that makes up part of the site 3 receptor binding epitope (Fig. 6A), which could lead to distinct binding topologies of site 3 receptors. Moreover, although the site 2 receptor binding epitope is located on helices A and C, which are more structurally conserved across the cytokines, different binding modes could still be adopted by the shared receptor for different cytokines. For example, although site 2 of CNTF, CLCF1, LIF, and IL-6 all engage gp130, the binding location of gp130 on LIF is apparently shifted to the N-terminal end of helix A compared to that of other cytokines, leading to an enlarged distance between the membrane-proximal domains of the two signaling receptors in the LIF complex. These different topologies of binding to various cytokines, together with divergent ways of engaging alpha receptors, lead to distinct angles and distances of the receptor juxtamembrane domains in different complexes (Fig. 7E). It is possible that these ectodomain topology differences of signaling receptors could be transmitted into the ICDs, which, in turn, affect the orientation or proximity of the JAK kinases bound to the ICDs of the receptors. As a result, this may alter JAK-mediated phosphorylation events on various STAT substrates and adaptors and lead to distinct gene expression profiles. In agreement with this hypothesis, engineered Epo-EpoR signaling complexes with different orientations or distances of receptor juxtamembrane domains induce distinct effects in hematopoiesis (*39*).

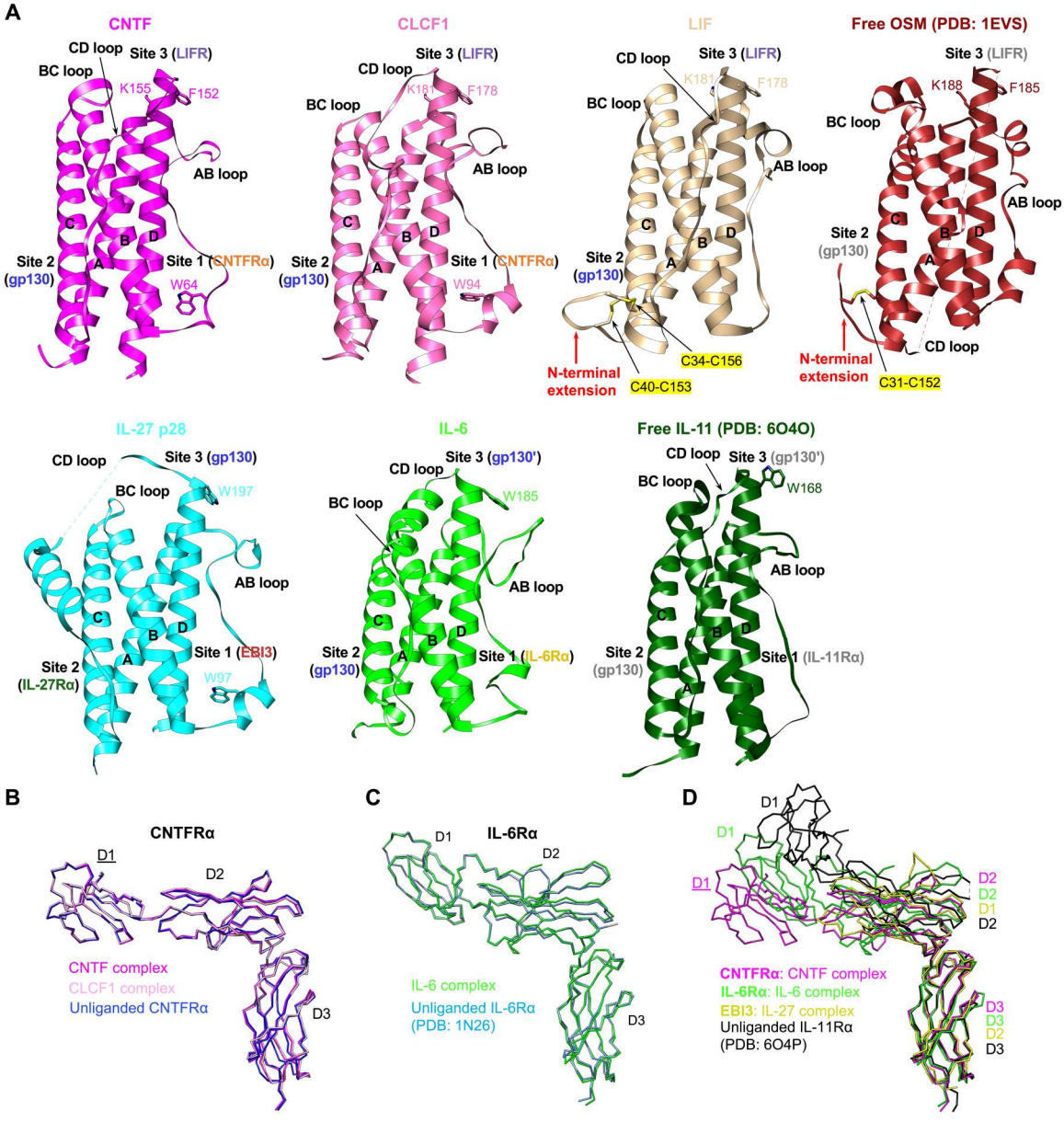

Fig. 6. Structural comparisons of cytokines and nonsignaling receptors in the gp130 family cytokine receptor complexes. (**A**) The structures of seven gp130 family cytokines are aligned on the four-helix bundle. Important conserved residues for binding to receptors at sites 1 and 3 are shown in stick form and labeled. LIF and OSM both have an N-terminal extension preceding helix A that is tethered to helix C by disulfide bonds (C34 to C156 and C40 to C153 for LIF; C31 to C152 for OSM). (**B**) Superposition of CNTFRα from the CNTF and CLCF1 signaling complex models containing full ECDs (Fig. 1, B and E) in which CNTFRα D1 is fitted as a rigid body (the label for D1 is underlined), as well as unliganded CNTFRα from the CNTFRα/REGN8938 Fab/H4H25322P2 Fab complex. All molecules are shown as C-alpha ribbon traces. (**C**) Superposition of IL-6Rα from the IL-6 signaling complex and unliganded IL-6Rα (PDB: 1N26). Both molecules are shown as C-alpha ribbon traces. (**D**) Superposition of liganded CNTFRα, IL-6Rα, and EBI3 from the CNTF, IL-6, and IL-27 signaling complexes, respectively, and unliganded IL-11Rα (PDB: 6O4P). All molecules are shown as C-alpha ribbon traces. The label for CNTFRα D1 is underlined to indicate that it is a rigid body–fitted domain in the CNTF complex model with full ECDs, as shown in Fig. 1B.

Difference in receptor-cytokine affinity and complex stability could be another factor that affects the biological specificities of the cytokines. Engineered IL-6 with lower affinity to gp130 was shown to decrease STAT1 phosphorylation more profoundly than STAT3 phosphorylation and thereby induce STAT3-biased responses (*43*). IL-13 variants with various affinities to receptors also cause different functional outputs (*44*). Both studies proposed that changes in cytokine-receptor affinities alter the stability of the signaling complex, which, in turn, affects receptor endocytosis that plays an important role in regulating STATs′ activation pattern. We found that the CLCF1 complex and IL-27 complex appear to be more unstable than the other signaling complexes we characterized since the particles imaged in the cryo-EM experiments for both samples showed a very low percentage of full complex (~2%). (The complexes on the EM grids might be destabilized by physical forces that are not experienced by the complexes assembled on cell

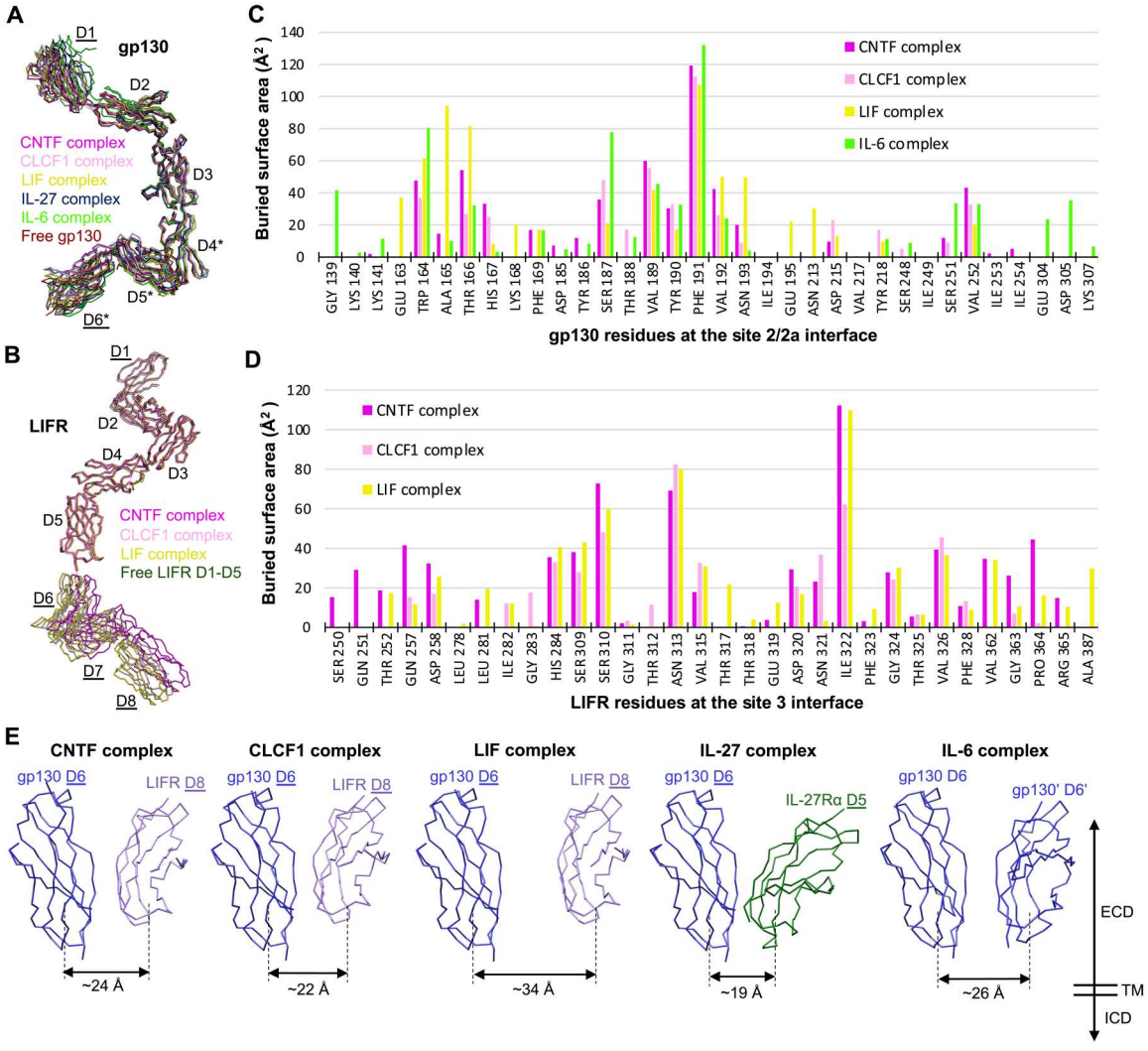

Fig. 7. Conformations of shared signaling receptors and relative positions of the receptor juxtamembrane domains in different gp130 family cytokine signaling complexes. (**A**) Superposition of gp130 from the CNTF, CLCF1, LIF, IL-27, and IL-6 signaling complexes, as well as free gp130 (PDB: 3L5H). All molecules are shown as C-alpha ribbon traces. The labels for gp130 D1 and D6 are underlined to indicate that they are rigid body–fitted domains in the CNTF, CLCF1, and LIF complex models with full ECDs; gp130 D4 to D6 (annotated by "*") are also rigid body–fitted domains in the IL-27 signaling complex model containing full ECDs. (**B**) Superposition of LIFR from the CNTF, CLCF1, and LIF signaling complexes, as well as free LIFR D1 to D5 (PDB: 3E0G). All molecules are shown as C-alpha ribbon traces. The labels for LIFR D1 and D6 to D8 are underlined to indicate that they are rigid body–fitted domains in the CNTF, CLCF1, and LIF complex models with full ECDs. (**C**) Histogram of buried surface area for gp130 residues at the site 2/2a interface in various signaling complexes. (**D**) Histogram of buried surface area for LIFR residues at the site 3 interface in various signaling complexes. (**E**) Relative positions of membrane-proximal domains of the two signaling receptors in different gp130 cytokine signaling complexes. All models are aligned on gp130 D6. The approximate distance between the bottom centers of the receptor juxtamembrane domains in each complex is indicated. All molecules are shown as C-alpha ribbon traces. The labels for gp130 D6 and LIFR D8 in the CNTF, CLCF1, and LIF complex, and gp130 D6 and IL-27Rα D5 in the IL-27 complex are underlined to indicate that they are rigid body–fitted domains in the corresponding complex models with full ECDs as shown in Figs. 1 (B, E, H) and 4B.

membrane.) A previous study has shown comparable affinities of CNTF sites 2 and 3 to gp130 and LIFR, respectively (*9*). However, a CNTF-CNTFRα-gp130 assembly intermediate was observed in our CNTF complex sample (fig. S2B), consistent with the observation in cells (*5*), suggesting that CNTF site 3 has relatively low receptor binding affinity compared with its site 2. Similarly, IL-27 p28 was also reported to have weaker site 3 binding affinity to gp130 than site 2 binding affinity to IL-27Rα (*14*, *25*), and a p28-EBI3-IL-27Rα intermediate was seen in our IL-27 complex sample (fig. S8B). In contrast, it has been shown that LIF has a much higher site 3 binding affinity to LIFR than site 2 binding affinity to gp130 (*12*), in agreement with the existence of LIF-LIFR assembly intermediate in our reconstituted LIF complex sample (fig. S5B) and in cells (*5*). We did not see the previously proposed IL-6-IL-6Rα-gp130 intermediate (*3*, *5*) in our IL-6 complex sample. It may be that this trimer intermediate only exists transiently and that the cooperative assembly mechanism of this complex rapidly promotes the formation of the final hexameric site 2 + 3 complex (*3*). These different relative binding affinities of the cytokine sites 2 and 3 to corresponding receptors in different signaling complexes could lead to variabilities in stability of these complexes and thus

contribute to biological specificities of different cytokines as previously proposed (*43*).

Since gp130 plays a key role in the signaling of multiple cytokines, pathogenic gp130 mutations have been reported to be associated with immunodeficiency diseases, such as hyper-IgE syndrome and Stüve-Wiedemann syndrome (*45*). The Uhlig group has identified several gp130 variants, including complete loss-of-function variants that impair all gp130-dependent signaling and homozygous missense variants that selectively affect signaling of the IL-6 family cytokines (*45*–*48*). Three point mutations, N404Y, P498L, and A517P, were identified at the gp130 D3-D4, D4-D5, and D5-D6 interfaces, respectively. While these mutations all significantly inhibited IL-6 and IL-11 signaling and resulted in partial-to-severe reduction of CNTF, CLCF1, IL-27, OSM, and CT-1 signaling, they barely or only partially impair LIF signaling (*45*–*47*). All-atom molecular dynamics simulations of the three gp130 variants suggested increased conformational flexibility at both the D3-D4 interface caused by the N404Y mutation and the D5-D6 interface due to the A517P mutation, and more subtle effect of the P498L mutation on the dynamics of the D4-D5 interface, consistent with the observation that the P498L variant showed more subtle defectiveness in pSTAT3 response compared with the other two variants (*45*). On the basis of our structures solved in this study, the LIF complex and the IL-27 complex have the longest (~34 Å) and shortest (~19 Å) distance between the signaling receptor juxtamembrane domains, respectively, while this distance in the CNTF, CLCF1, and IL-6 complex is in the middle range (around 25 Å) (Fig. 7E). We propose that these differences in receptor juxtamembrane domain distance in different native signaling complexes could be one reason for the selective effects of the pathogenic gp130 mutations on the signaling of various cytokines. Since LIF can still signal when its two receptors gp130 and LIFR are relatively far away from each other, it might have a higher threshold to tolerate the flexibility of gp130 membrane-proximal domains induced by the pathogenic gp130 mutations. In contrast, both IL-6 and IL-11 signal through gp130 homodimerization, which means that the mutation-induced dynamics of gp130 will be amplified as both signaling complexes have two copies of gp130. Therefore, IL-6 and IL-11 might have a much lower tolerance to the pathogenic gp130 mutations compared with other cytokines that signal through gp130 heterodimerization with another receptor. However, future structural studies of these signaling complexes reconstituted with the reported pathogenic gp130 variants are required to provide a definitive explanation for the selective response of these gp130 variants to different cytokines.

Our attempts to resolve the TM region of gp130 in the IL-6 signaling complex reconstituted in detergent were not very successful because of high mobility of the TM region in the detergent micelle relative to the complex extracellular portion, presumably because there is a flexible linker (~15 Å in length) between gp130 D6 and the TM helix. This inherent flexibility of gp130 TM region was also observed in other single-pass TM receptors, such as IR and IGF1R (*34*, *35*), and might be important for the engagement of the two TM helices embedded in the dynamic membrane environment and the subsequent positioning and activation of the JAK molecules bound to the two receptor ICDs. To draw clearer conclusions regarding signal transduction of the gp130 family cytokine signaling complexes, it might be necessary to obtain high-resolution structures of these complexes using full-length signaling receptors solubilized in detergent or in a nanodisc membrane, ideally with JAK kinase bound to the cytoplasmic portion, which might restrain the flexibility of the TM domain.

CRLF1 is known to be critical for CLCF1 secretion, but its role in CLCF1 signaling remains elusive. It was shown that the two key CLCF1 residues (F178 and K181) engaging LIFR are also important for binding to CRLF1, suggesting that CRLF1 and LIFR compete for binding to CLCF1 site 3, and thereby, CLCF1 may need to be released from CRLF1 for signaling (*19*). Another study reported that CRLF1 is able to form a tripartite complex with CLCF1 and CNTFRα and promote CLCF1 signaling by sustaining CLCF1 binding to CNTFRα (*23*). However, our structure of the CRLF1-CLCF1-CNTFRα complex shows that CLRF1 does not contact CNTFRα directly, and CNTFRα is not required for CLCF1-mediated CRLF1 dimerization. Unexpectedly, CLCF1 sites 2 and 3 are engaged by two CRLF1 molecules analogous to how they are engaged by gp130 and LIFR in the CLCF1 signaling complex, supporting the model that CLCF1 has to dissociate from CRLF1 to bind to gp130 and LIFR to form a functional signaling complex (*19*). The mechanism for CLCF1 release from CRLF1 in cells remains to be investigated.

Together, our structures of the gp130 family cytokine receptor complexes expand our view of the signaling mechanism of this family and provide valuable insights for therapeutically targeting gp130-mediated signaling pathways. On the basis of the detailed cytokine receptor contacts described above, it may be possible to generate chimeric cytokines, agonists, or antagonists via structure-guided protein engineering. The geometry of the full extracellular portion of each signaling complex could also guide the design of therapeutics, such as bispecific antibodies to bring the signaling receptors together in a conformation that mimics the natural cytokine signaling complex. Engineered molecules such as these will hopefully be valuable in treating diseases arising from disorders in gp130-mediated signaling.

MATERIALS AND METHODS

Protein purification

All proteins used in this study were recombinant human proteins. The residues of all proteins mentioned here were numbered on the basis of UniProt sequences; the signal peptides were counted in the numbering. The following proteins were all C-terminal myc-myc-His–tagged secreted proteins expressed in Chinese hamster ovary (CHO-K1) cells: gp130 ectodomain (amino acids E23-E619, REGN2669), LIFR ectodomain (amino acids Q45-S833, REGN3269), CNTFRα (amino acids Q23-S342)-GGGPG-CNTF (amino acids M1-I186) fusion protein (REGN3637), CNTFRα (amino acids Q23-S342, REGN3000), IL-27Rα ectodomain (amino acids Q33-K516, REGN9497), EBI3 (amino acids R21-K229)-$(GGGGS)_4$-p28 (amino acids F29-P243) fusion protein (REGN5948), and IL-6Rα ectodomain (amino acids L20-M331, REGN78). Filtered cell culture supernatants containing target proteins were buffer-exchanged through dialysis against Dulbecco's phosphate-buffered saline (DPBS) and loaded onto preequilibrated Talon columns (Clontech, no. 635682). After washing the columns with DPBS containing 500 mM NaCl, followed by a second wash with DPBS plus 500 mM NaCl and 5 mM imidazole, the proteins were eluted with DPBS plus 500 mM NaCl and 200 mM imidazole. The eluates were dialyzed against DPBS with 5% glycerol, and,

subsequently, the proteins were further purified by size-exclusion chromatography (SEC). The proteins were concentrated and frozen for future use. IL-6 (amino acids V30-M212, REGN125) was expressed as an inclusion body in *Escherichia coli* and refolded into a soluble form.

Human gp130 with full ectodomain, TM domain, and cytoplasmic Box1/2 region linked to an hFc tag [(gp130 E23-D700)-$(GGGGS)_3$-hFc] was expressed in the Expi293 expression system (Thermo Fisher Scientific). The cell pellet was homogenized in lysis buffer [PBS + 1% n-dodecyl-β-maltoside (DDM) detergent]. Clarified lysate was loaded onto a hand-packed MabSelect SuRe (Cytiva) column. The column was washed with lysis buffer and then PBS with 0.02% DDM (Anatrace). Bound gp130 protein was eluted four times with batches of two-column volume elution buffer containing 100 mM glycine (pH 2.7), 150 mM NaCl, and 0.02% DDM into tubes containing 1 ml of 1 M tris-Cl (pH 8.0) for neutralization. Fractions were analyzed by SDS–polyacrylamide gel electrophoresis (SDS-PAGE), and gp130-containing fractions were combined and dialyzed against buffer containing 20 mM Hepes (pH 7.4), 150 mM NaCl, 5% glycerol, and 0.02% DDM. The protein was further concentrated with a 100-kDa molecular weight cutoff (MWCO) centrifugal concentrator and flash-frozen in liquid nitrogen for future use. Before complex formation, the detergent-solubilized gp130 protein was further purified over a Superose 6 increase 10/300 GL gel filtration column equilibrated with 50 mM tris (pH 7.5), 150 mM NaCl, and 0.02% glyco-diosgenin (Anatrace), and concentrated with a 100-kDa MWCO centrifugal concentrator.

Three other proteins were purchased from R&D Systems, including CNTFRα (amino acids Q23-P346)-GSGSSRGGSGSGGSGGGGSKL-CLCF1 (L28-F225) fusion protein (no. 2415-CR) and CRLF1 (amino acids A38-R422)/CLCF1 (amino acids L28-F225) complex protein (no. 1151-CL) purified from mouse myeloma cell line NS0, and LIF (amino acids P24 to F202, no. 7734-LF) purified from *E. coli*. The SEC and SDS-PAGE analysis data for these proteins are summarized in fig. S1.

Fab fragment preparation

Two anti-CNTFRα antibodies, REGN8938 and H4H25311P2, were digested into $F(ab')^2$ and Fc fragments using Fabricator enzyme (Genovis), following instructions from the manufacturer. $F(ab')^2$ was reduced into F(ab)′ using 2-mercaptoethylamine (Thermo Fisher Scientific) followed by Fc fragment removal using the CaptureSelect IgG-Fc (ms) affinity resin (Thermo Fisher Scientific). F(ab)′ fragments were further purified over a Superdex 200 increase 10/300 GL gel filtration column equilibrated with 50 mM tris (pH 7.5) and 150 mM NaCl and concentrated using a 10-kDa MWCO centrifugal concentrator. The SEC and SDS-PAGE analysis data for the two antibody Fab fragments are summarized in fig. S1.

Complex preparation

All complexes were reconstituted by mixing the corresponding components at an equal molar ratio followed by incubation at 4°C for 1 hour as follows: CNTF complex (gp130 ectodomain, LIFR ectodomain, and CNTFRα-CNTF fusion protein), CNTFRα/REGN8938 Fab/H4H25311P2 Fab complex (CNTFRα, REGN8938 Fab, and H4H25311P2 Fab), CLCF1 complex (gp130 ectodomain, LIFR ectodomain, and CNTFRα-CLCF1 fusion protein), CRLF1/CLCF1/CNTFRα complex (CRLF1/CLCF1 complex and CNTFRα), LIF complex (gp130 ectodomain, LIFR ectodomain, and LIF), IL-27 complex (gp130 ectodomain, IL-27Rα ectodomain, and EBI3-p28 fusion protein), and IL-6 complex (gp130 solubilized in detergent, IL-6Rα ectodomain, and IL-6).

The CNTF complex, CLCF1 complex, LIF complex, IL-27 complex, and CRLF1/CLCF1/CNTFRα complex were further purified over a Superdex 200 increase 10/300 GL gel filtration column equilibrated with 50 mM tris (pH 7.5) and 150 mM NaCl. Peak fractions containing the target complex were collected and concentrated to ~2.5 mg/ml using a 30-kDa MWCO centrifugal concentrator. The SEC and SDS-PAGE analysis data for these complexes are summarized in fig. S1.

Cryo-EM sample preparation and data collection

Each freshly purified complex was mixed with ~0.15% amphipol PMAL-C8 (Anatrace) immediately before pipetting 3.5 μl of the mixture onto an UltrAufoil R1.2/1.3, 300 mesh grid (Quantifoil). The grid was blotted for 4 s at a force of 0 and plunge-frozen into liquid ethane using a Vitrobot Mark IV (Thermo Fisher Scientific) operated at 4°C and 100% humidity. The grid was then loaded into a Titan Krios G3i microscope (Thermo Fisher Scientific) equipped with a K3 camera and energy filter (Gatan) for data collection in counted mode at a nominal magnification of 105,000× using the EPU software (Thermo Fisher Scientific). Each movie contained 46 dose fractions over a 2-s exposure, and the total acquired dose per $Å^2$ was ~40 electrons. CNTF complex, CNTFRα/REGN8938 Fab/H4H25311P2 Fab complex, and IL-6 complex had a pixel size of 0.85 Å, while all other complexes had a pixel size of 0.86 Å. All movies had a defocus range of −1.4 to −2.6 μm. The total number of movies collected for each sample was as follows: CNTF complex (6511), CNTFRα/REGN8938 Fab/H4H25311P2 Fab complex (7859), CLCF1 complex (25,442), CRLF1/CLCF1/CNTFRα complex (9943), CRLF1/CLCF1 complex (7275), LIF complex (11,007), IL-27 complex (26,610), and IL-6 complex (12,143). Cryo-EM data collection statistics are also summarized in table S2.

Cryo-EM data processing

Cryo-EM data were processed using cryoSPARC v2 (*49*). Movies were motion-corrected by Patch motion correction, and contrast transfer function (CTF) parameters were estimated by Patch CTF estimation. Particles were initially picked using Blob picker from ~500 micrographs to generate two-dimensional (2D) class averages to be used as templates for the subsequent template picking. Junk particles were removed by multiple rounds of 2D classification, followed by ab initio reconstruction, homogeneous refinement, and heterogeneous refinement to identify the best class of particles representing the target protein complex. These particles were further refined using nonuniform refinement (*50*) and/or local refinement to generate the final cryo-EM density map. Cryo-EM data processing statistics are summarized in table S2.

For the CNTF signaling complex, 3,197,974 particles were picked by template picking (fig. S2). A total of 778,622 particles were left after 2D classification, which were subjected to ab initio reconstruction to isolate a class of 250,735 "good" particles. Nonuniform refinement of these particles led to a 3.03-Å map, which has well-resolved interaction core region but fragmented LIFR D6 to D8 density. This map was used for manual model building and all-atom real-space refinement of the assembly core region (CNTF,

CNTFRα D2D3, gp130 D2 to D5, and LIFR D2 to D5). These particles were further subjected to heterogeneous refinement, identifying 100,013 particles with more homogeneous LIFR D6 to D8 domains. Nonuniform refinement of this subset of particles yielded another map with lower global resolution (3.37 Å) but improved LIFR D6 to D8 density. This map was used to generate a more complete model for the full extracellular portion of the CNTF signaling complex.

For the CNTFRα/REGN8938 Fab/H4H25311P2 Fab complex, 4,515,671 particles were picked by template picking (fig. S3). A total of 1,046,202 particles were left after 2D classification, which were subjected to ab initio reconstruction to isolate a class of 665,975 good particles. Homogeneous refinement of these particles led to a 3.14-Å map, which was further subjected to heterogeneous refinement, identifying a subset of 568,328 particles. Nonuniform refinement of these particles yielded a final map with a global resolution of 2.93 Å.

For the CLCF1 signaling complex, 13,119,612 particles were picked by template picking (fig. S4). A total of 202,209 particles were left after 2D classification, which were subjected to ab initio reconstruction to isolate a class of 92,463 good particles. Homogeneous refinement of these particles led to a 4.37-Å map, which was further subjected to nonuniform refinement, generating a final map with a global resolution of 3.90 Å.

For the LIF signaling complex, 5,545,456 particles were picked by template picking (fig. S5). A total of 726,434 particles were left after 2D classification, which were subjected to ab initio reconstruction to isolate a class of 410,979 good particles. Homogeneous refinement of these particles led to a 3.66-Å map, which was further subjected to heterogeneous refinement, identifying a subset of 171,328 particles. Nonuniform refinement of these particles yielded a final map with a global resolution of 3.54 Å.

For the CRLF1/CLCF1/CNTFRα complex, 1,258,062 particles were picked by template picking (fig. S6). A total of 203,337 particles were left after 2D classification, which were subjected to ab initio reconstruction to isolate a class with 138,937 good particles contributing to a 3D reconstruction with clear twofold symmetry. Homogeneous refinement of these particles with C2 symmetry imposed led to a 3.52-Å map, which was further subjected to heterogeneous refinement, identifying a subset of 117,773 particles. Nonuniform refinement of these particles with C2 symmetry imposed generated a final map with a global resolution of 3.40 Å.

For the CRLF1/CLCF1 complex, 1,504,984 particles were picked by template picking (fig. S7). A total of 369,658 particles were left after 2D classification, which were subjected to ab initio reconstruction to isolate a class with 204,227 good particles contributing to a 3D reconstruction with clear twofold symmetry. Homogeneous refinement of these particles with C2 symmetry imposed led to a 3.66-Å map, which was further subjected to nonuniform refinement with C2 symmetry imposed, yielding a final map with a global resolution of 3.45 Å.

For the IL-27 signaling complex, 19,480,836 particles were picked by template picking (fig. S8). A total of 429,793 particles were left after 2D classification, which were subjected to ab initio reconstruction to isolate a class of 139,752 good particles. Homogeneous refinement of these particles resulted in a 4.70-Å map, which was further subjected to nonuniform refinement to generate a map with a global resolution of 4.14 Å. This map was used to generate a model for the full extracellular portion of the IL-27 signaling complex. The assembly core region of the complex, including p28, EBI3, gp130 D1 to D3, and IL-27Rα D1 to D2, was further subjected to particle subtraction and local refinement using a soft mask around this region, yielding an improved local map with 3.81-Å overall resolution, which was used for model building and all-atom real-space refinement of the assembly core region.

For the detergent-solubilized IL-6 signaling complex, 3,881,621 particles were picked by template picking (fig. S9). A total of 324,482 particles were left after 2D classification, which were subjected to ab initio reconstruction to isolate a class with 224,163 good particles contributing to a 3D reconstruction with clear twofold symmetry. Homogeneous refinement of these particles with C2 symmetry imposed led to a 3.26-Å map, which was further subjected to heterogeneous refinement, identifying a subset of 105,760 particles. Nonuniform refinement of these particles with C2 symmetry imposed generated a final map with a global resolution of 3.22 Å.

Model building and refinement

The published structures of gp130 D1 to D6 [Protein Data Bank (PDB): 3L5H] (*2*), LIFR D1 to D5 (PDB: 3E0G) (*9*), CNTF (PDB: 1CNT) (*51*), CNTFRα D3 (PDB: 1UC6) (*52*), LIF/gp130 D2D3 (PDB: 1PVH) (*12*), IL-6Rα D1 to D3 (PDB: 1N26) (*53*), and IL6/IL-6Rα D2D3/gp130 D1 to D3 (PDB: 1P9M) (*3*), as well as AlphaFold-predicted models of CLCF1, CRLF1, EBI3, p28, and IL27-Rα, were used as initial models for model building. A combination of picked initial models (or selected domains of these models) was docked into corresponding cryo-EM density map using the Fit-in-map function of UCSF Chimera (*54*). The models were adjusted manually in Coot (*55*), followed by real-space refinement with secondary structure and noncrystallographic symmetry restraints in Phenix (*56*). The geometries of the models were validated by using MolProbity (*57*) in Phenix, and the statistics are summarized in table S2. Fully real space–refined atomic models were obtained for all regions of the CNTFRα/REGN8938 Fab/H4H25311P2 Fab complex, the CRLF1/CLCF1/CNTFRα complex, and the IL-6 signaling complex extracellular portion. For the CNTF, CLCF1, LIF, and IL-27 signaling complexes, only the well-resolved regions around the interaction core of each complex (CNTF, CNTFRα D2D3, gp130 D2 to D5, and LIFR D2 to D5 of the CNTF complex; CLCF1, CNTFRα D2D3, gp130 D2 to D5, and LIFR D2 to D5 of the CLCF1 complex; LIF, gp130 D2 to D5, and LIFR D2 to D5 of the LIF complex; and IL-27 p28, EBI3, IL-27Rα D1D2, and gp130 D1 to D3 of the IL-27 complex) were manually modeled and real space–refined. These manually built and all-atom real space–refined structures, which were deposited to PDB, were further subjected to PDBePISA analysis (*58*) to identify residue-residue interactions (shown in Figs. 2, 3, and 5) and calculate buried surface areas of individual residues or all residues at each binding interface (shown in Figs. 1 to 5, and 7).

Models containing full ECDs of the CNTF, CLCF1, LIF, and IL-27 signaling complex were also generated by combining the above-mentioned structures of the interaction core region and models of the receptor distal domains, which were derived from published structures (gp130 D1, PDB: 1P9M; gp130 D6, PDB: 3L5H; gp130 D4 to D6, PDB: 3L5H; and LIFR D1, PDB: 3E0G), a structure obtained in this study (CNTFRα D1, fig. S3), or AlphaFold-predicted models (LIFR D6 to D8 and IL-27Rα D3 to D5). Briefly, the models of the receptor distal domains were docked into the corresponding density with the guidance of available receptor structures/

AlphaFold models using the Fit-in-map function of Chimera, followed by connection of these models to the structures of the complex interaction core region in Coot. The composite models with full ECDs were further real space–refined against corresponding cryo-EM maps using the rigid-body strategy in Phenix. These models containing rigid body–fitted receptor distal domains, which were not deposited to PDB, were used to present the overall architectures of the extracellular portions of these complexes and relative positions of the membrane-proximal domains (shown in Figs. 1, 4, and 7). All structural figures here were made in UCSF Chimera.

Supplementary Materials

This PDF file includes:

Figs. S1 to S10
Tables S1 and S2

View/request a protocol for this paper from *Bio-protocol*.

REFERENCES AND NOTES

1. S. Kang, M. Narazaki, H. Metwally, T. Kishimoto, Historical overview of the interleukin-6 family cytokine. *J. Exp. Med.* **217**, e20190347 (2020).
2. Y. Xu, N. J. Kershaw, C. S. Luo, P. Soo, M. J. Pocock, P. E. Czabotar, D. J. Hilton, N. A. Nicola, T. P. J. Garrett, J. G. Zhang, Crystal structure of the entire ectodomain of gp130: Insights into the molecular assembly of the tall cytokine receptor complexes. *J. Biol. Chem.* **285**, 21214–21218 (2010).
3. M. J. Boulanger, D. C. Chow, E. E. Brevnova, K. C. Garcia, Hexameric structure and assembly of the interleukin-6/IL-6 α-receptor/gp130 complex. *Science* **300**, 2101–2104 (2003).
4. S. Davis, T. H. Aldrich, D. M. Valenzuela, V. Wong, M. E. Furth, S. P. Squinto, G. D. Yancopoulos, The receptor for ciliary neurotrophic factor. *Science* **253**, 59–63 (1991).
5. S. Davis, T. H. Aldrich, N. Stahl, L. Pan, T. Taga, T. Kishimoto, N. Y. Ip, G. D. Yancopoulos, LIFRβ and gp130 as heterodimerizing signal transducers of the tripartite CNTF receptor. *Science* **260**, 1805–1808 (1993).
6. G. C. Elson, E. Lelièvre, C. Guillet, S. Chevalier, H. Plun-Favreau, J. Froger, I. Suard, A. B. de Coignac, Y. Delneste, J. Y. Bonnefoy, J. F. Gauchat, H. Gascan, CLF associates with CLC to form a functional heteromeric ligand for the CNTF receptor complex. *Nat. Neurosci.* **3**, 867–872 (2000).
7. T. Huyton, J. G. Zhang, C. S. Luo, M. Z. Lou, D. J. Hilton, N. A. Nicola, T. P. J. Garrett, An unusual cytokine:Ig-domain interaction revealed in the crystal structure of leukemia inhibitory factor (LIF) in complex with the LIF receptor. *Proc. Natl. Acad. Sci. U.S.A.* **104**, 12737–12742 (2007).
8. S. Pflanz, J. C. Timans, J. Cheung, R. Rosales, H. Kanzler, J. Gilbert, L. Hibbert, T. Churakova, M. Travis, E. Vaisberg, W. M. Blumenschein, J. D. Mattson, J. L. Wagner, W. To, S. Zurawski, T. K. McClanahan, D. M. Gorman, J. F. Bazan, R. de Waal Malefyt, D. Rennick, R. A. Kastelein, IL-27, a heterodimeric cytokine composed of EBI3 and p28 protein, induces proliferation of naive $CD4^+$ T cells. *Immunity* **16**, 779–790 (2002).
9. G. Skiniotis, P. J. Lupardus, M. Martick, T. Walz, K. C. Garcia, Structural organization of a full-length gp130/LIF-R cytokine receptor transmembrane complex. *Mol. Cell* **31**, 737–748 (2008).
10. G. Skiniotis, M. J. Boulanger, K. C. Garcia, T. Walz, Signaling conformations of the tall cytokine receptor gp130 when in complex with IL-6 and IL-6 receptor. *Nat. Struct. Mol. Biol.* **12**, 545–551 (2005).
11. N. Stahl, T. J. Farruggella, T. G. Boulton, Z. Zhong, J. E. Darnell Jr., G. D. Yancopoulos, Choice of STATs and other substrates specified by modular tyrosine-based motifs in cytokine receptors. *Science* **267**, 1349–1353 (1995).
12. M. J. Boulanger, A. J. Bankovich, T. Kortemme, D. Baker, K. C. Garcia, Convergent mechanisms for recognition of divergent cytokines by the shared signaling receptor gp130. *Mol. Cell* **12**, 577–589 (2003).
13. N. A. Caveney, C. R. Glassman, K. M. Jude, N. Tsutsumi, K. C. Garcia, Structure of the IL-27 quaternary receptor signaling complex. *eLife* **11**, (2022).
14. Y. Jin, P. K. Fyfe, S. Gardner, S. Wilmes, D. Bubeck, I. Moraga, Structural insights into the assembly and activation of the IL-27 signaling complex. *EMBO Rep.* **23**, e55450 (2022).
15. J. Jumper, R. Evans, A. Pritzel, T. Green, M. Figurnov, O. Ronneberger, K. Tunyasuvunakool, R. Bates, A. Žídek, A. Potapenko, A. Bridgland, C. Meyer, S. A. A. Kohl, A. J. Ballard, A. Cowie, B. Romera-Paredes, S. Nikolov, R. Jain, J. Adler, T. Back, S. Petersen, D. Reiman, E. Clancy, M. Zielinski, M. Steinegger, M. Pacholska, T. Berghammer, S. Bodenstein, D. Silver, O. Vinyals, A. W. Senior, K. Kavukcuoglu, P. Kohli, D. Hassabis, Highly accurate protein structure prediction with AlphaFold. *Nature* **596**, 583–589 (2021).
16. F. Rousseau, S. Chevalier, C. Guillet, E. Ravon, C. Diveu, J. Froger, F. Barbier, L. Grimaud, H. Gascan, Ciliary neurotrophic factor, cardiotrophin-like cytokine, and neuropoietin share a conserved binding site on the ciliary neurotrophic factor receptor alpha chain. *J. Biol. Chem.* **283**, 30341–30350 (2008).
17. N. Panayotatos, E. Radziejewska, A. Acheson, R. Somogyi, A. Thadani, W. A. Hendrickson, N. Q. McDonald, Localization of functional receptor epitopes on the structure of ciliary neurotrophic factor indicates a conserved, function-related epitope topography among helical cytokines. *J. Biol. Chem.* **270**, 14007–14014 (1995).
18. A. Di Marco, I. Gloaguen, R. Graziani, G. Paonessa, I. Saggio, K. R. Hudson, R. Laufer, Identification of ciliary neurotrophic factor (CNTF) residues essential for leukemia inhibitory factor receptor binding and generation of CNTF receptor antagonists. *Proc. Natl. Acad. Sci. U.S.A.* **93**, 9247–9252 (1996).
19. D. Perret, C. Guillet, G. Elson, J. Froger, H. Plun-Favreau, F. Rousseau, M. Chabbert, J. F. Gauchat, H. Gascan, Two different contact sites are recruited by cardiotrophin-like cytokine (CLC) to generate the CLC/CLF and CLC/sCNTFRalpha composite cytokines. *J. Biol. Chem.* **279**, 43961–43970 (2004).
20. F. Rousseau, J. F. Gauchat, J. G. McLeod, S. Chevalier, C. Guillet, F. Guilhot, I. Cognet, J. Froger, A. F. Hahn, P. M. Knappskog, H. Gascan, H. Boman, Inactivation of cardiotrophin-like cytokine, a second ligand for ciliary neurotrophic factor receptor, leads to cold-induced sweating syndrome in a patient. *Proc. Natl. Acad. Sci. U.S.A.* **103**, 10068–10073 (2006).
21. J. W. Kim, C. P. Marquez, R. A. P. Sperberg, J. Wu, W. G. Bae, P. S. Huang, E. A. Sweet-Cordero, J. R. Cochran, Engineering a potent receptor superagonist or antagonist from a novel IL-6 family cytokine ligand. *Proc. Natl. Acad. Sci. U.S.A.* **117**, 14110–14118 (2020).
22. K. R. Hudson, A. B. Vernallis, J. K. Heath, Characterization of the receptor binding sites of human leukemia inhibitory factor and creation of antagonists. *J. Biol. Chem.* **271**, 11971–11978 (1996).
23. J. V. Larsen, A. M. Kristensen, L. T. Pallesen, J. Bauer, C. B. Vægter, M. S. Nielsen, P. Madsen, C. M. Petersen, Cytokine-like factor 1, an essential facilitator of cardiotrophin-like cytokine: Ciliary neurotrophic factor receptor α signaling and sorLA-mediated turnover. *Mol. Cell. Biol.* **36**, 1272–1286 (2016).
24. D. Chow, X. He, A. L. Snow, S. Rose-John, K. C. Garcia, Structure of an extracellular gp130 cytokine receptor signaling complex. *Science* **291**, 2150–2155 (2001).
25. F. Rousseau, L. Basset, J. Froger, N. Dinguirard, S. Chevalier, H. Gascan, IL-27 structural analysis demonstrates similarities with ciliary neurotrophic factor (CNTF) and leads to the identification of antagonistic variants. *Proc. Natl. Acad. Sci. U.S.A.* **107**, 19420–19425 (2010).
26. J. S. Stumhofer, E. D. Tait, W. J. Q. III, N. Hosken, B. Spudy, R. Goenka, C. A. Fielding, A. C. O'Hara, Y. Chen, M. L. Jones, C. J. M. Saris, S. Rose-John, D. J. Cua, S. A. Jones, M. M. Elloso, J. Grötzinger, M. P. Cancro, S. D. Levin, C. A. Hunter, A role for IL-27p28 as an antagonist of gp130-mediated signaling. *Nat. Immunol.* **11**, 1119–1126 (2010).
27. R. D. Metcalfe, E. Hanssen, K. Y. Fung, K. Aizel, C. C. Kosasih, C. O. Zlatic, L. Doughty, C. J. Morton, A. P. Leis, M. W. Parker, P. R. Gooley, T. L. Putoczki, M. D. W. Griffin, Structures of the interleukin 11 signalling complex reveal dynamics of gp130 extracellular domains and the inhibitory mechanism of a cytokine variant.*bioRxiv*, 2022.2007.2021.500383 , (2022).
28. M. C. Deller, K. R. Hudson, S. Ikemizu, J. Bravo, E. Y. Jones, J. K. Heath, Crystal structure and functional dissection of the cytostatic cytokine oncostatin M. *Structure* **8**, 863–874 (2000).
29. R. D. Metcalfe, K. Aizel, C. O. Zlatic, P. M. Nguyen, C. J. Morton, D. S. S. Lio, H. C. Cheng, R. C. J. Dobson, M. W. Parker, P. R. Gooley, T. L. Putoczki, M. D. W. Griffin, The structure of the extracellular domains of human interleukin 11α receptor reveals mechanisms of cytokine engagement. *J. Biol. Chem.* **295**, 8285–8301 (2020).
30. T. L. Putoczki, R. C. Dobson, M. D. Griffin, The structure of human interleukin-11 reveals receptor-binding site features and structural differences from interleukin-6. *Acta Crystallogr. D Biol. Crystallogr.* **70**, 2277–2285 (2014).
31. B. Schuster, M. Kovaleva, Y. Sun, P. Regenhard, V. Matthews, J. Grötzinger, S. Rose-John, K.-J. Kallen, Signaling of human ciliary neurotrophic factor (CNTF) revisited. The interleukin-6 receptor can serve as an alpha-receptor for CTNF. *J. Biol. Chem.* **278**, 9528–9535 (2003).
32. C. Garbers, B. Spudy, S. Aparicio-Siegmund, G. H. Waetzig, J. Sommer, C. Hölscher, S. Rose-John, J. Grötzinger, I. Lorenzen, J. Scheller, An interleukin-6 receptor-dependent molecular switch mediates signal transduction of the IL-27 cytokine subunit p28 (IL-30) via a gp130 protein receptor homodimer. *J. Biol. Chem.* **288**, 4346–4354 (2013).
33. R. S. Syed, S. W. Reid, C. Li, J. C. Cheetham, K. H. Aoki, B. Liu, H. Zhan, T. D. Osslund, A. J. Chirino, J. Zhang, J. Finer-Moore, S. Elliott, K. Sitney, B. A. Katz, D. J. Matthews, J. J. Wendoloski, J. Egrie, R. M. Stroud, Efficiency of signalling through cytokine receptors depends critically on receptor orientation. *Nature* **395**, 511–516 (1998).

34. E. Uchikawa, E. Choi, G. Shang, H. Yu, X. C. Bai, Activation mechanism of the insulin receptor revealed by cryo-EM structure of the fully liganded receptor-ligand complex. *eLife* **8**, (2019).
35. J. Li, E. Choi, H. Yu, X. C. Bai, Structural basis of the activation of type 1 insulin-like growth factor receptor. *Nat. Commun.* **10**, 4567 (2019).
36. C. R. Glassman, N. Tsutsumi, R. A. Saxton, P. J. Lupardus, K. M. Jude, K. C. Garcia, Structure of a Janus kinase cytokine receptor complex reveals the basis for dimeric activation. *Science* **376**, 163–169 (2022).
37. I. Kurth, U. Horsten, S. Pflanz, A. Timmermann, A. Küster, H. Dahmen, I. Tacken, P. C. Heinrich, G. Müller-Newen, Importance of the membrane-proximal extracellular domains for activation of the signal transducer glycoprotein 130. *J. Immunol.* **164**, 273–282 (2000).
38. A. Timmermann, A. Kuster, I. Kurth, P. C. Heinrich, G. Muller-Newen, A functional role of the membrane-proximal extracellular domains of the signal transducer gp130 in heterodimerization with the leukemia inhibitory factor receptor. *Eur. J. Biochem.* **269**, 2716–2726 (2002).
39. K. Mohan, G. Ueda, A. R. Kim, K. M. Jude, J. A. Fallas, Y. Guo, M. Hafer, Y. Miao, R. A. Saxton, J. Piehler, V. G. Sankaran, D. Baker, K. C. Garcia, Topological control of cytokine receptor signaling induces differential effects in hematopoiesis. *Science* **364**, (2019).
40. S. Yuzawa, Y. Opatowsky, Z. Zhang, V. Mandiyan, I. Lax, J. Schlessinger, Structural basis for activation of the receptor tyrosine kinase KIT by stem cell factor. *Cell* **130**, 323–334 (2007).
41. S. Markovic-Mueller, E. Stuttfeld, M. Asthana, T. Weinert, S. Bliven, K. N. Goldie, K. Kisko, G. Capitani, K. Ballmer-Hofer, Structure of the full-length VEGFR-1 extracellular domain in complex with VEGF-A. *Structure* **25**, 341–352 (2017).
42. J. S. Stumhofer, J. S. Silver, A. Laurence, P. M. Porrett, T. H. Harris, L. A. Turka, M. Ernst, C. J. M. Saris, J. J. O'Shea, C. A. Hunter, Interleukins 27 and 6 induce STAT3-mediated T cell production of interleukin 10. *Nat. Immunol.* **8**, 1363–1371 (2007).
43. J. Martinez-Fabregas, S. Wilmes, L. Wang, M. Hafer, E. Pohler, J. Lokau, C. Garbers, A. Cozzani, P. K. Fyfe, J. Piehler, M. Kazemian, S. Mitra, I. Moraga, Kinetics of cytokine receptor trafficking determine signaling and functional selectivity. *eLife* **8**, (2019).
44. I. Moraga, D. Richter, S. Wilmes, H. Winkelmann, K. Jude, C. Thomas, M. M. Suhoski, E. G. Engleman, J. Piehler, K. C. Garcia, Instructive roles for cytokine-receptor binding parameters in determining signaling and functional potency. *Sci. Signal.* **8**, ra114 (2015).
45. Y. H. Chen, D. B. Zastrow, R. D. Metcalfe, L. Gartner, F. Krause, C. J. Morton, S. Marwaha, L. Fresard, Y. Huang, C. Zhao, C. McCormack, D. Bick, E. A. Worthey, C. M. Eng, J. Gold, Undiagnosed Diseases Network, S. B. Montgomery, P. G. Fisher, E. A. Ashley, M. T. Wheeler, M. W. Parker, V. Shanmugasundaram, T. L. Putoczki, D. Schmidt-Arras, A. Laurence, J. A. Bernstein, M. D. W. Griffin, H. H. Uhlig, Functional and structural analysis of cytokine-selective IL6ST defects that cause recessive hyper-IgE syndrome. *J. Allergy Clin. Immunol.* **148**, 585–598 (2021).
46. T. Schwerd, S. R. F. Twigg, D. Aschenbrenner, S. Manrique, K. A. Miller, I. B. Taylor, M. Capitani, S. J. McGowan, E. Sweeney, A. Weber, L. Chen, P. Bowness, A. Riordan, A. Cant, A. F. Freeman, J. D. Milner, S. M. Holland, N. Frede, M. Müller, D. Schmidt-Arras, B. Grimbacher, S. A. Wall, E. Y. Jones, A. O. M. Wilkie, H. H. Uhlig, A biallelic mutation in IL6ST encoding the GP130 co-receptor causes immunodeficiency and craniosynostosis. *J. Exp. Med.* **214**, 2547–2562 (2017).
47. T. Shahin, D. Aschenbrenner, D. Cagdas, S. K. Bal, C. D. Conde, W. Garncarz, D. Medgyesi, T. Schwerd, B. Karaatmaca, P. G. Cetinkaya, S. Esenboga, S. R. F. Twigg, A. Cant, A. O. M. Wilkie, I. Tezcan, H. H. Uhlig, K. Boztug, Selective loss of function variants in IL6ST cause hyper-IgE syndrome with distinct impairments of T-cell phenotype and function. *Haematologica* **104**, 609–621 (2019).
48. Y. H. Chen, G. Grigelioniene, P. T. Newton, J. Gullander, M. Elfving, A. Hammarsjö, D. Batkovskyte, H. S. Alsaif, W. I. Y. Kurdi, F. Abdulwahab, V. Shanmugasundaram, L. Devey, S. Bacrot, J. Brodszki, C. Huber, B. Hamel, D. Gisselsson, N. Papadogiannakis, K. Jedrycha, B. Gürtl-Lackner, A. S. Chagin, G. Nishimura, D. Aschenbrenner, F. S. Alkuraya, A. Laurence, V. Cormier-Daire, H. H. Uhlig, Absence of GP130 cytokine receptor signaling causes extended Stüve-Wiedemann syndrome. *J. Exp. Med.* **217**, (2020).
49. A. Punjani, J. L. Rubinstein, D. J. Fleet, M. A. Brubaker, cryoSPARC: Algorithms for rapid unsupervised cryo-EM structure determination. *Nat. Methods* **14**, 290–296 (2017).
50. A. Punjani, H. Zhang, D. J. Fleet, Non-uniform refinement: Adaptive regularization improves single-particle cryo-EM reconstruction. *Nat. Methods* **17**, 1214–1221 (2020).
51. N. Q. McDonald, N. Panayotatos, W. A. Hendrickson, Crystal structure of dimeric human ciliary neurotrophic factor determined by MAD phasing. *EMBO J.* **14**, 2689–2699 (1995).
52. D. Man, W. He, K. H. Sze, K. Gong, D. K. Smith, G. Zhu, N. Y. Ip, Solution structure of the C-terminal domain of the ciliary neurotrophic factor (CNTF) receptor and ligand free associations among components of the CNTF receptor complex. *J. Biol. Chem.* **278**, 23285–23294 (2003).
53. J. N. Varghese, R. L. Moritz, M. Z. Lou, A. van Donkelaar, H. Ji, N. Ivancic, K. M. Branson, N. E. Hall, R. J. Simpson, Structure of the extracellular domains of the human interleukin-6 receptor α-chain. *Proc. Natl. Acad. Sci. U.S.A.* **99**, 15959–15964 (2002).
54. E. F. Pettersen, T. D. Goddard, C. C. Huang, G. S. Couch, D. M. Greenblatt, E. C. Meng, T. E. Ferrin, UCSF Chimera—A visualization system for exploratory research and analysis. *J. Comput. Chem.* **25**, 1605–1612 (2004).
55. P. Emsley, B. Lohkamp, W. G. Scott, K. Cowtan, Features and development of Coot. *Acta Crystallogr. D Biol. Crystallogr.* **66**, 486–501 (2010).
56. D. Liebschner, P. V. Afonine, M. L. Baker, G. Bunkóczi, V. B. Chen, T. I. Croll, B. Hintze, L. W. Hung, S. Jain, A. J. McCoy, N. W. Moriarty, R. D. Oeffner, B. K. Poon, M. G. Prisant, R. J. Read, J. S. Richardson, D. C. Richardson, M. D. Sammito, O. V. Sobolev, D. H. Stockwell, T. C. Terwilliger, A. G. Urzhumtsev, L. L. Videau, C. J. Williams, P. D. Adams, Macromolecular structure determination using x-rays, neutrons and electrons: Recent developments in Phenix. *Acta. Crystallogr. D. Struct. Biol.* **75**, 861–877 (2019).
57. C. J. Williams, J. J. Headd, N. W. Moriarty, M. G. Prisant, L. L. Videau, L. N. Deis, V. Verma, D. A. Keedy, B. J. Hintze, V. B. Chen, S. Jain, S. M. Lewis, W. B. Arendall III, J. Snoeyink, P. D. Adams, S. C. Lovell, J. S. Richardson, D. C. Richardson, MolProbity: More and better reference data for improved all-atom structure validation. *Protein Sci.* **27**, 293–315 (2018).
58. E. Krissinel, K. Henrick, Inference of macromolecular assemblies from crystalline state. *J. Mol. Biol.* **372**, 774–797 (2007).

Acknowledgments: We thank J. C. Lin, M. Sleeman, E. Goebel, and L. McGoldrick for critical reading of the manuscript; J. Yanolatos for project management; J. Altarejos for discussion of the project; Y. Shen for early discussion on model building of the CNTF signaling complex; and O. Olsen for help with the submission of the manuscript. We thank Regeneron TP-Protein Development and PMPD teams for purification and analytical characterization of most protein components used in this study. **Funding:** This project has been funded by Regeneron Pharmaceuticals. **Author contributions:** Y.Z., P.E.S., G.D.Y., A.J.M., M.W.S., W.C.O., and M.C.F. conceptualized the studies. Y.Z. prepared complexes, acquired cryo-EM data, processed data, and built and refined the atomic models, with contributions from K.S. and M.C.F. P.E.S. and J.C. contributed most of the reagents. J.W., A.G.Z., and S.H. conceptualized the IL-27 signaling complex study and analyzed the IL-27 complex structural data. G.D.Y., A.J.M., M.W.S., W.C.O., and M.C.F. analyzed data and supervised the whole project. Y.Z. drafted the manuscript, which was edited and finalized with contributions of all authors. **Competing interests:** Regeneron authors own options and/or stock of the company. P.E.S. is an author on U.S. provisional patent application 63/368,201, filed 12 July 2022 by Regeneron Pharmaceuticals, covering the two anti-CNTFR antibodies described in this work. G.D.Y., A.J.M., M.W.S., and W.C.O. are officers of Regeneron. The authors declare that they have no other competing interests. **Data and materials availability:** All data needed to evaluate the conclusions in the paper are present in the paper and/or the Supplementary Materials. The cryo-EM density maps and corresponding atomic coordinates of all complexes described here have been deposited to Protein Data Bank [(PDB) https://www.rcsb.org/] and Electron Microscopy Data Bank [(EMDB) https://www.ebi.ac.uk/emdb/], respectively. The corresponding PDB and EMDB identification numbers are as follows: CNTF signaling complex (8D74, EMD-27227/EMD-27229), CLCF1 signaling complex (8D7R, EMD-27231), LIF signaling complex (8D6A, EMD-27221), IL-27 signaling complex (8D85, EMD-27247/EMD-27246), IL-6 signaling complex (8D82, EMD-27244), CRLF1/CLCF1/CNTFRα complex (8D7H, EMD-27230), and CNTFRα/REGN8938 Fab/H4H25311P2 Fab complex (8D7E, EMD-27228). Regeneron materials described here may be made available to qualified, academic, noncommercial researchers through a material transfer agreement upon request at https://regeneron.envisionpharma.com/vt_regeneron/. For questions about how Regeneron shares materials, use the email address preclinical.collaborations@regeneron.com.

Submitted 17 August 2022
Accepted 10 February 2023
Published 17 March 2023
10.1126/sciadv.ade4395